A Spectral Rotary Analysis of Gravity Waves: An Application during one of the SOUTHTRAC Flights

A. de la Torre[1], P. Alexander[2], T. Marcos[1], R. Hierro[1], P. Llamedo[1], J.L. Hormaechea[3], P. Preusse[4], M. Geldenhuys[4,5], L. Krasauskas[4], A. Giez[6], B. Kaifler[7], N. Kaifler[7] and M. Rapp[7,8]

[1]LIDTUA(CIC) and CONICET, Facultad de Ingeniería, Universidad Austral, Pilar, Argentina.

[2]Instituto de Física de Buenos Aires, CONICET, Buenos Aires, Argentina.

[3] Estación Astrónomica Río Grande, Facultad de Ciencias Astronómicas y Geofísicas, Universidad Nacional de La Plata, and CONICET, La Plata, Argentina.

[4]Institute of Energy and Climate Research (IEK-7), ForschungszentrumJülich, Jülich, Germany.

[5]South African Weather Service, Private Bag X097, Pretoria 0001, South Africa.

[6]Einrichtung Flugexperimente, Deutsches Zentrum für Luft- und Raumfahrt, Oberpfaffenhofen, Germany.

[7]Institut für Physik der Atmosphäre, Deutsches Zentrum für Luft- und Raumfahrt, Oberpfaffenhofen, Germany.

[8]Meteorologisches Institut München, Ludwig-Maximilians-Universität München, Munich, Germany.

Correspondingauthor: Alejandro de la Torre (adelatorre@austral.edu.ar)

Key Points:

- A rotary spectral analysis is proposed to classify possible sources of gravity waves according to their degree of polarization.
- From reanalysis data, the method is applied at a selected position during one of the flights of the SOUTHTRAC-GWExperiment.
- Upward and downward gravity wave structures from orographic and non-orographic origin with different degrees of polarization are observed.

Abstract

To understand the main orographic and non-orographic sources of gravity waves (GWs) over South America during an Experiment (Rapp et al, 2021, https://doi.org/10.1175/BAMS-D-20-0034.1), we propose the application of a rotational spectral analysis based on methods originally developed for oceanographic studies. This approach is deployed in a complex scenario of large-amplitude GWs by applying it to reanalysis data. We divide the atmospheric region of interest into two height intervals. The simulations are compared with lidar measurements during one of the flights. From the degree of polarization and the total energy of the GWs, the contribution of the upward and downward wave packets is described as a function of their vertical wavenumbers. At low levels, a larger downward energy flux is observed in a few significant harmonics, suggesting inertial GWs radiated at polar night jet levels, and below, near to a cold front. In contrast, the upward GW energy flux, per unit area, is larger than the downward flux, as expected over mountainous areas. The main sub-regions of upward GW energy flux are located above Patagonia, the Antarctic Peninsula and only some oceanic sectors. Above the sea, there are alternating sub-regions dominated by linearly polarized GWs and sectors of downward GWs. At the upper levels, the total available GW energy per unit mass is higher than at the lower levels. Regions with different degrees of polarization are distributed in elongated bands. A satisfactory comparison is made with an analysis based on the phase difference between temperature and vertical wind disturbances.

Plain Language Summary

Atmospheric gravity waves (GWs) are of great importance in the transport of energy and momentum through the atmosphere. Their sources can be broadly classified as stationary and non-stationary. The southern tip of South America represents one of the most important natural laboratories for detecting the coexistence of large-amplitude GWs. We present a spectral method to establish a semi-quantitative classification of the different groups of GWs and their main vertical direction of propagation. We apply the method on the basis of global model data.We divide the lower and middle atmosphere into two vertical intervals and compare the model with data from one of the instruments deployed during the experiment. From the degree of polarization of the GWs, we describe the net contribution of the upward and downward wave packets as a function of their spectral harmonics. The main subregions of upward gravity wave

energy flux alternate with subregions dominated by linearly polarized GWs and downward gravity wave sectors mainly above the ocean. At the upper levels, the total available GW energy per unit mass is higher than at the lower levels. A comparison is made between these results and an independent analysis based on the known polarization relations for GWs.

1 Introduction

The complex structure inherent to frequently observed atmospheric gravity wave (GW) ensembles constitutes a challenge that remains difficult to address (e.g., P. Alexander et al., 2015a, b; de la Torre et al., 2019; Fritts & M.J. Alexander, 2003; Wickert et al., 2020). This is mainly due to the time and space constraints imposed by the observational windows and by the complexity of the atmospheric wave structures and other present phenomena (M.J. Alexander, 1998; Wu et al., 2006). The following basic classification of the main GW sources are: the flow of the air forced by the orography (called mountain waves (MWs)), atmospheric convection, and the spontaneous emission after geostrophic adjustment of the flow in the vicinity of jets and fronts (Fritts & M.J. Alexander, 2003; Plougonven& Zhang, 2014; Zhang et al., 2004). In particular, the usual assumption describes a scenario with dominant monochromatic linear GWs, which would explain the transport of large fractions of the wave energy and momentum flux through different atmospheric levels and synoptic conditions.

In a relatively simple GW scenario, the hodographic technique (see e.g.,Gubenko et al., 2020; Vincent, 1984) requires a single coherent wave leading to the fluctuations that perturb the horizontal velocity profile. For a single, linear, steady, non-dissipating, elliptically polarized wave in a region with negligible vertical shear in the background wind (Eckermann, 1996), the intrinsic frequency of the GWs can be obtained by the axial ratio of the ellipse (Cot& Barat, 1986), its horizontal propagation axis by the orientation of the ellipse major axis (Vincent &Fritts, 1987) and the direction of the GWs vertical group velocity by the sense of ellipse rotation with height (Hirota& Niki,1985). However, Eckermann & Hocking (1989) demonstrated that hodographic analyses of profiles that contained a large number of GWs sometimes yielded results that reflected the statistical properties of random incoherent fluctuations, rather than the polarization characteristics. Nevertheless, the isolation and characterization of GWs when the wave field consists mainly of a few monochromatic waves are quite straightforward.

From another perspective, spectral techniques allow searching for coherent waves within various traceable wavelength bands. These methods are especially useful when the distribution of GW energy is broadly assigned to wave packets with very different wavelengths, frequencies and amplitudes (e.g., Hines, 1991). This may be a typical scenario in the geographic region considered in this study. The analysis of the polarization characteristics of the GW spectrum may provide a valuable semi-quantitative characterization of the GW ensemble (Eckermann, 1996; Gonella, 1972; Leaman & Sanford, 1975; Mooers, 1973), specifically their dominant intrinsic frequencies or wavelengths, vertical propagation direction of GW and GW energy and momentum fluxes. This approach has been applied in the past to oceanic GWs (e.g., Leaman & Sanford, 1975).

A classification of GWs by their sources is proposed: orographic (linearly polarized (LP)) or non-orographic (elliptically polarized (EP)). This classification is based on their degree of polarization. As is well known, the degree of polarization also corresponds to non-hydrostatic, hydrostatic non-rotating or rotating GWs, following their intrinsic frequency regimes (e.g. Gill, 1982, Section 8.8). From For the polarization relations for the complex amplitudes of the zonal and meridional perturbation velocity components (Vadas, 2013 –equation (B3); P. Alexander et al., 2022 –equation (1)), it may be seen that an ellipse links both horizontal velocity components, whereby the eccentricity equals the ratio of GW inertial to intrinsic frequency. As the eccentricity lies between 0 and 1, a value close to 1 indicates a wave linearly polarized, which corresponds to an intrinsic frequency close to the buoyancy frequency, within the non-hydrostatic regime. An alternative to this proposal may be to rely on their time dependence (stationary or non-stationary, respectively). In the present analysis, we will illustratively apply the method considering model simulations with high spatial resolution at a fixed time. We leave the time dependence classification based on mesoscale simulations for a future contribution.

The geographic region considered in this study includes the southern Andes, Patagonia, the Antarctic Peninsula and the surrounding oceanic areas. It exhibits the world's strongest hotspots of GW activity, taking place mainly during austral winter and early spring (e.g., P. Alexander et al., 2010; de la Torre et al., 2012; Fritts et al., 2016; Hoffmann et al., 2013; Llamedo et al., 2019; Rapp et al., 2021). An intense MW activity was observed by other studies above and to the lee of the mountains, given the prevailing strong tropospheric westerly winds. Strong GW

activity is observed in the middle to upper stratosphere along 60°S, from the Drake Passage to the South Pacific (see, e.g., Ern et al., 2006; Hindley et al., 2015; M. J. Alexander et al., 2010]. This circumpolar belt of almost zonally symmetric GW activity is related to strong momentum fluxes and is sometimes referred to as the GW belt.

A precursory experiment to the one referred in this study, also performed in the southern hemisphere in winter, was the Deep Propagating GW Experiment (DEEPWAVE) (Fritts et al., 2016). It was conducted by several research flights with two aircraft from Christchurch, New Zealand, involving various ground-based instruments, satellite datasets, and a variety of numerical models (Bramberger et al., 2017; Fritts et al., 2016; Gisinger et al., 2017; Portele et al., 2018; Smith et al., 2016).The Southern Hemisphere Transport, Dynamics, and Chemistry–Gravity Waves (SOUTHTRAC-GW) mission, performed in September 2019, was based on a synchronized multiple experimental platform. During this experiment, the complexity of the interacting ensemble of GW activity below the mesopause, at extratropical southern latitudes was again observed, as expected (Rapp et al. 2021).The experiment consisted in deploying three main instruments dedicated to the measurement of GW signatures. In particular, the Airborne Lidar for Middle Atmosphere research (ALIMA), a compact upward-pointing Rayleigh lidar using a pulsed neodymium-doped yttrium aluminum garnet laser (Kaifler et al., 2020). The campaign objectives are described in Rapp et al (2021).SOUTHTRAC-GW was the first airborne field campaign devoted to GW dynamics in the atmosphere from the troposphere up to the mesopause (5 to 80 km altitude) in the region considered here (Rapp et al., 2021). During the experiment, 7 successful flights spanning a total of 60 hr were completed. The campaign period coincided with the occurrence of a sudden stratospheric warming which created critical level conditions at about 40 km altitude (Dörnbrack et al, 2020). Among many parameters, measurements from temperature (T) and zonal (u), meridional (v) and vertical (w) wind components were obtained. A preliminary analysis of the measurements and model results revealed strong evidence for MW excitation over the Andes and subsequent vertical as well as horizontal propagation, including refraction and downwind advection into the polar night jet and along the GW belt (Rapp et al., 2021).

In order to interpret the observations, the sources of GWs and their propagation direction is very important. Our main aim, after describing a rotary spectral method capable of detecting the

spatial distribution of dominant up- and down going GW energy, is to apply it to a SOUTHTRAC case study. We selected one of the first flights, identified as ST08, performed from 11 September at 23:05:36 UTC to 12 September 2019 at 07:21:14 UTC (Rapp et al., 2021). The The method is based on the determination of the dominant degree of polarization of the GW ensemble, as a function of the vertical wavenumber, height interval and geographic sector, above the southern Patagonia, Drake Passage and Antarctic Peninsula. Stationary waves are expected to be mostly linearly polarized (LP) and are included in the analysis. The method is illustrated for a fixed time selected after the beginning of one of the HALO flights, when the reanalysis data are available. ST08 was the flight with the best conditions for excitation and deep mountain wave propagation and we chose the time when HALO crossed the highest mountains for our reanalysis. The selected altitude ranges include the tropospheric and stratospheric regions.

Section 2 introduces the spectral rotary method. In Section 3, the model and experimental data, the expected limitations derived from the observational windows and the available time and space resolution are described. The synoptic conditions and a validation of the simulated T profile against the lidar data are performed at the fixed selected time. In section 4, the rotary spectra method is applied to reanalysis data at a representative HALO position during one of the SOUTHTRAC-GW flights. We separate the region considered into two non-overlapping tropo-stratospheric and strato-mesospheric altitude intervals. The flight considered in this study reveals an unusually deep propagation of stationary GWs up to mesospheric levels. In section 5, a comparison is made with an independent method consisting in the calculation of the phase differences between T and wperturbations (T' and w') and from there, the associated vertical horizontal momentum flux. Section 6 provides a discussion and some conclusions that should also be taken into account in future analyses and remaining case studies of the SOUTHTRAC-GW Experiment.

2 Spectral rotary analysis (SRA)

As pointed out by Eckermann (1999), three statistical approaches may be used to characterize the polarization ellipses defined from horizontal wind velocity perturbation data: the hodographic method analysis (e.g., Cadet &Teitelbaum, 1979; Cot & Barat 1986; Vincent, 1984; Vincent & M. J. Alexander, 2020), the cross-spectral analysis (e.g., Cho, 1995), and the spectral rotary

analysis (e.g., Eckermann & Vincent, 1989). As stated by Eckermann (1999), all three methods are in some sense equivalent. The appropriate choice will probably depend on the scenario.

One particularly general form of the hodographic method is a description in terms of the so-called Stokes parameters (e.g., Vincent & Fritts, 1987). This is an analysis technique derived from the electromagnetic waves theory and is well described in many standard textbooks (e.g., Mishchenko, 2014). According to this method, any partially polarized wave motion can be described completely and uniquely in terms of its Stokes parameters. Vincent & Fritts (1987) applied such parameters in GW studies. The method assumes that any vertical profile of horizontal wind velocity perturbations contains a partially polarized coherent wave field embedded in an unpolarized, isotropic, noise-like background velocity field. The latter is characterized by a variance equal to the sum of the average of u' and v' variances and a phase accounting for the elliptical nature of the wave. If this phase is 0° or 180°, it implies a linear polarization, 90° or 270° implies a circular polarization and any value in between implies an elliptical polarization. The perturbation velocity vector will rotate anticyclonically with time and space as one moves in a direction opposite to the phase velocity (Gill, 1982; Placke et al., 2013). In the southern hemisphere, this means that upgoing waves (downward phase progression) account for a wind vector that rotates anticlockwise with increasing height, while with downgoing waves, a clockwise rotation is expected (Vincent, 1984). For atmospheric scenarios with undeniably complex distributions of coexisting wavepackets, a spectral approach should be undertaken, in order to recognize the statistically meaningful processes lying within.

In the process, a rotary-vector analysis method may be developed based on the assembly of a complex vector consisting of 2 components of the velocity vector along perpendicular axes, in particular, the zonal and meridional wind components (e.g., Gonella, 1972; Mooers, 1973). Below, we adapted the mentioned developments to our purpose. After a Fourier transform of the horizontal zonal and meridional residual wind components u' and v':

$$u'(z) = \frac{\pi}{2}\int_0^\infty [\mathrm{B}_1(\mathrm{m})\cos(\mathrm{mz}) + \mathrm{B}_2(\mathrm{m})\sin(\mathrm{mz})]\,dm \qquad (1)$$

and

198 $$v'(z) = \frac{\pi}{2}\int_0^\infty [\mathrm{B}_3(\mathrm{m})\cos(\mathrm{mz}) + \mathrm{B}_4(\mathrm{m})\sin(\mathrm{mz})]\,dm \quad (2)$$

199 the spectral method gives the decomposition of the total available wave energy in terms of the
200 so-called clockwise and anticlockwise spectra, as a function of the vertical wavenumber (m). In
201 the present analysis, we choose the vertical z coordinate increasing downwards, following a
202 convention in the above mentioned previous spectral analyses in the ocean. That is, z = 0 at the
203 highest point of each of the two altitude ranges selected below. If one considers the horizontal
204 velocity vector to be u + iv, where u is the east (real) part of the horizontal velocity and v is the
205 north (imaginary) part, then, at each m, we can represent the above helix simply by:

206 $$u_m + iv_m = u_+ e^{imz} + u_- e^{-imz} \quad (3)$$

207 with complex constants u_+ and u_-.

208 Then, it may be shown that (e.g., Gonella, 1972):

209 $$|u_+| = \frac{1}{2}[(\mathrm{B}_4 + \mathrm{B}_1)^2 + (\mathrm{B}_3 - \mathrm{B}_2)^2]^{1/2} \quad (4)$$

210 and

211 $$|u_-| = \frac{1}{2}[(\mathrm{B}_4 - \mathrm{B}_1)^2 + (\mathrm{B}_3 + \mathrm{B}_2)^2]^{1/2} \quad (5)$$

212 The anticlockwise and clockwise components of the energy per unit mass spectrum are given by:

213 $$S_+ = \frac{1}{2}(u_+^* u_+) \quad (6)$$

214 and

215 $$S_- = \tfrac{1}{2}(u_-^* u_-) \quad (7)$$

216 The integration over m under S_+ and S_- shows the relative contribution of each energy
217 component. It provides the partition of the total energy. However, it must be stressed that this is
218 an overestimation of the energy associated with the upgoing and downgoing waves. Low-
219 frequency GWs are not exactly circularly polarized except near the inertial frequency, but

elliptically polarized. Since an elliptically polarized wave can always be resolved into clockwise and anticlockwise circularly polarized components, even a purely upgoing or downgoing wave will contribute to both the clockwise and the anticlockwise spectra. In this sense, this analysis must not be considered as strictly quantitative. Nevertheless, useful statistical information regarding the prevailing up- or down-propagating GW packets may be obtained and, based only on the nature of their polarization, their probable sources can be identified.

For the present analysis, we define the total rotational energy as

$$E_T = S_- + S_+ \tag{8}$$

In turn, the difference

$$C_R = S_- - S_+ \tag{9}$$

will be defined here as the 'rotary coefficient'. It is proportional to the average surface of the ellipse. Its sign indicates the dominant polarization of the ellipse: positive for clockwise, negative for anticlockwise. Then, a positive/negative C_R value means clockwise/counterclockwise rotation with increasing z (namely, counterclockwise/clockwise with increasing altitude).

Additionally, sometimes it is convenient to define the 'normalized rotary coefficient', as it is bounded in the interval [-1, 1]:

$$NC_R = (S_- - S_+)/(S_- + S_+) \tag{10}$$

In effect, its magnitude will be +/- 1 for pure rotary motion and zero for unidirectional (linearly polarized) motion. To set this out, we write $S_+ = p\, S_-$, with p real and ≥ 0, $NC_R = (S_- - p\, S_-) / (S_- + p\, S_-) = (1 - p)/(1 + p)$.

Next, we calculate and plot C_R and NC_R, as they provide complementary information. For example, for a given vertical wavenumber m and altitude interval, a latitude-longitude sector with positive/negative C_R will reveal dominant up-/down-propagating GWs. Besides, if C_R is close to zero, this may indicate two possible structures: i) the presence of linearly polarized orographic GWs ($S_- \approx S_+$) or ii) a low total GW energy, where any polarization is possible.

Accordingly, for i), NC_R will be close to but different from zero and if ii), any NC_R value may be expected.

3 **IFS model reanalysis and experimental data: a case study**

The Integrated Forecasting System (IFS) of the European Centre for Medium-Range Weather Forecasts (ECMWF) is a global, hydrostatic, semi-implicit, semi-Lagrangian model for numerical weather prediction (horizontal resolution: 0.1°x0.1° (e.g., Polichtchouk et al., 2021). Perturbations of temperature, zonal, meridional and vertical wind velocity were inferred by subtraction from vertical profiles of T, u, v, w with a low pass cutoff at 15 km. GWs are considered to be well represented in IFS analyses up to an altitude of 55 km (Ehard et al., 2015). At higher altitudes, the simulated wave activity is damped within the model's sponge layer for numerical reasons.

The ALIMA lidar system was located onboard the German research aircraft HALO. It yields atmospheric density profiles in the altitude range from 20 to 90 km. T between 20 and 80 km altitude is obtained with varying degrees of accuracy. From 20-60 km, 60-70 km and 70-80 km, the corresponding error is 0.9, 2.9, and 6.5 K respectively. To separate GW induced temperature perturbations from atmospheric background temperatures, a 30 min running mean is applied.

The seven HALO flights designed for the study of GW dynamics took off from Río Grande. Each of them travelled along a trajectory typically around 7000 km.

The synoptic conditions for Flight 08 were dominated by a sudden stratospheric warming (SSW) that was present during September 2019, as described by Dörnbrack et al (2020). Although it was a weak event (Rapp et al., 2021), it affected the propagation conditions for MWs. In Figure 1a, the equivalent potential temperature shows a cold front at 850 hPa around 45-50°S. After 12 hours (Figure 1b), the air mass has been displaced to the north leaving the continent at lower levels. At 200 hPa, the streamlines field shows a deepening of the 850 trough with an almost in-phase N-S axis (Figure 1c) with a displacement to the east of the axis of the trough and an almost divergent flow over southern Patagonia (Figure 1d).

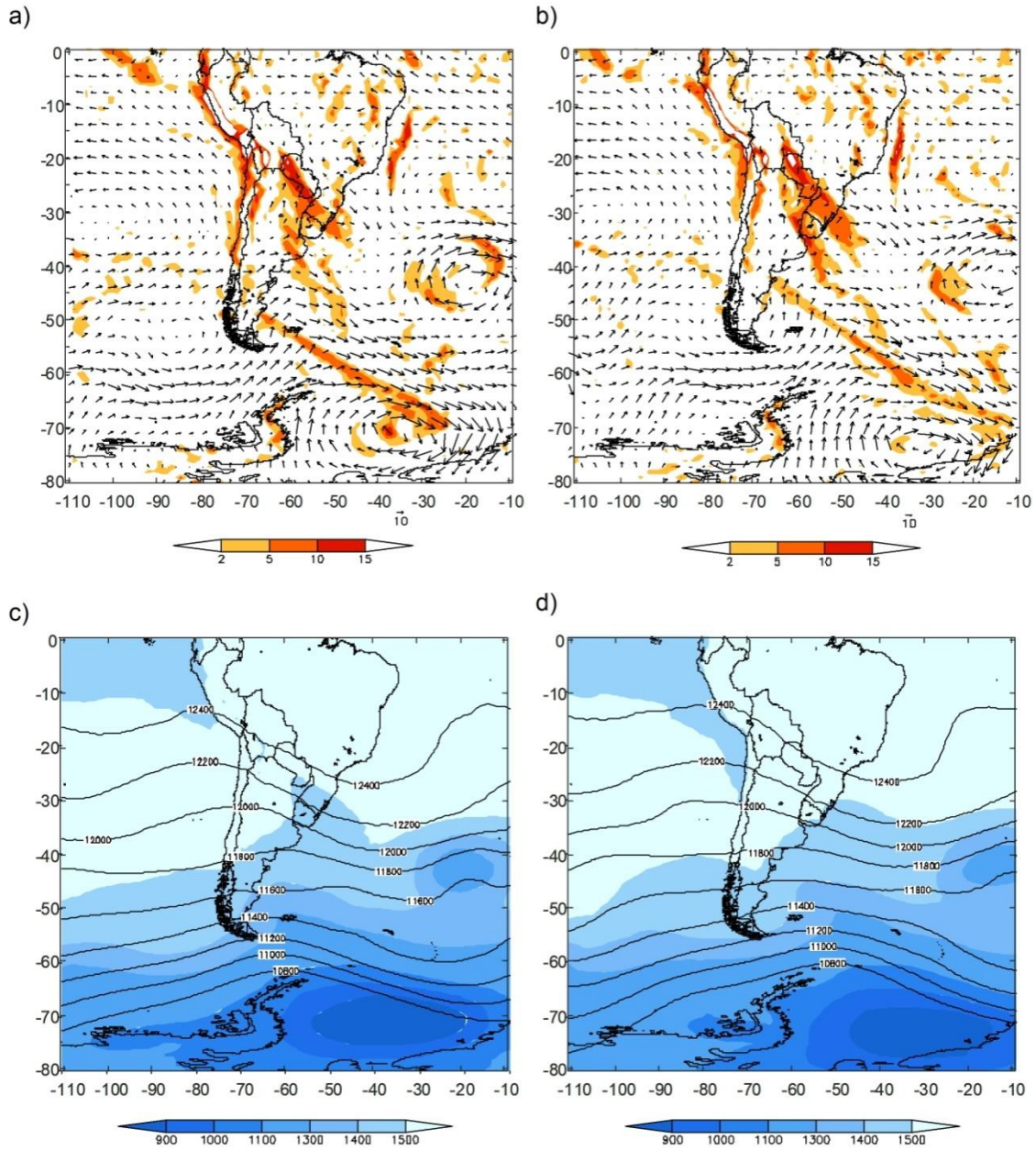

Figure 1. Synoptic conditions from NCEP on September 12, 2019. Equivalent potential temperature [K] at a) 00 UTC and b) 12 UTC. Geopotential height [m] at c) 00 UTC and d) 12 UTC. Isolines correspond to 200 hPa and colorbar to 850 hPa.

The trajectory followed by HALO during this flight is shown in Figure 2. Taking into account the takeoff time and duration of this flight, below we will consider IFS simulations available within this interval, on 12 September, 00UTC. Six segments (or legs) from this flight may be identified, on the basis of their lengths and constant direction and pressure levels. The latitude-longitude coordinates corresponding to the extremities of each leg are provided in Table 1.

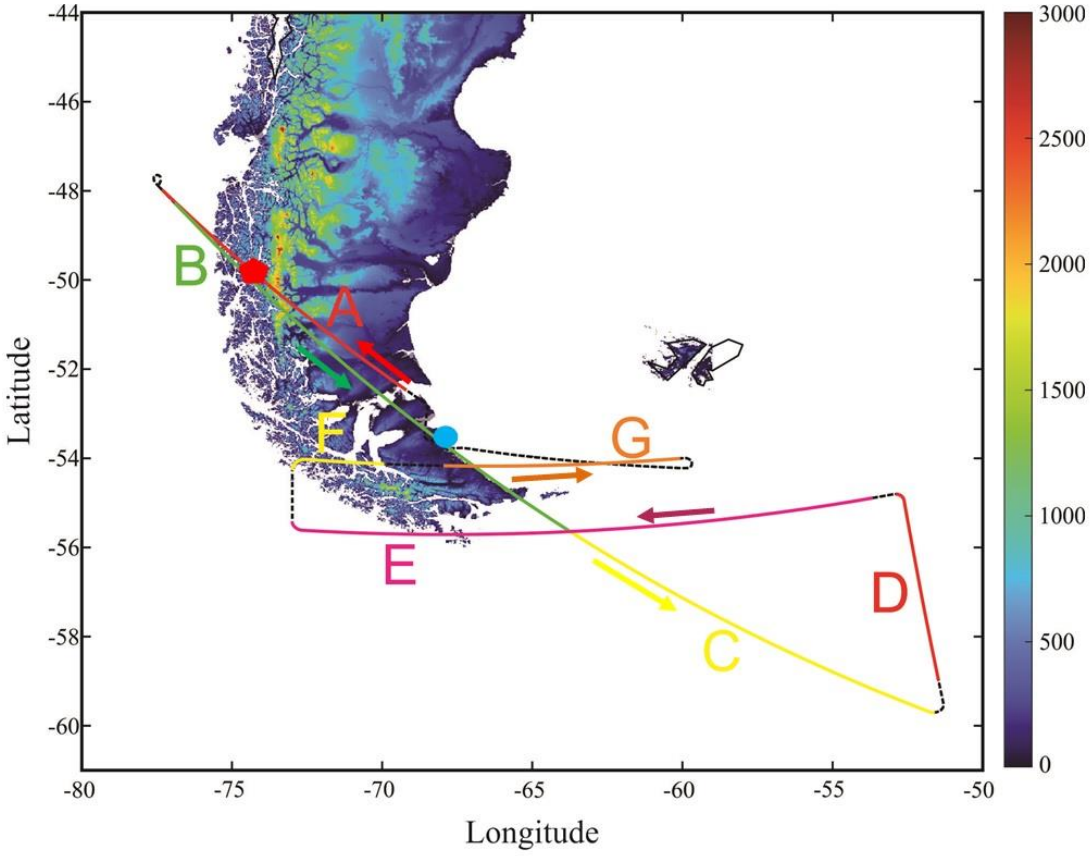

Figure 2. Trajectory of HALO flight ST08 during SOUTHTRAC-GW Mission performed on 11/12 September 2019. The position of the aircraft at 00:00 UTC on 12 September is indicated by the red pentagon. Seven segments (named from A to G - Table 1), correspond to seven constant pressure altitude legs followed by HALO. The orographic height is indicated in the colorbar [m]. HALO's takeoff location at Río Grande is shown by the blue circle.

Leg	Initiallatitude	Final latitude	Initiallongitude	Final longitude	Staticpressure [hPa]	Pressure altitude [Giez et al 2017] [m]	Beginning (min)	End (min)
A	**52.47° S**	**47.99° S**	**69.20° W**	**77.31° W**	**238.3**	**10670**	**0**	**59**
B	**48.27° S**	**55.62° S**	**76.91° W**	**63.78° W**	**178.2**	**12510**	**69**	**149**
C	**55.62° S**	**59.70° S**	**63.78° W**	**51.63° W**	**178.2**	**12510**	**149**	**201**

D	**58.97° S**	**54.80° S**	**51.47° W**	**52.85° W**	**161.7**	**13130**	**208**	**245**
E	**54.89° S**	**55.42° S**	**53.66° W**	**73.00° W**	**147.1**	**13740**	**250**	**355**
F	**54.26° S**	**54.12° S**	**73.00° W**	**69.97° W**	**147.1**	**13740**	**363**	**376**
G	**54.17° S**	**54.01° S**	**67.96° W**	**60.12° W**	**133.6**	**14340**	**384**	**415**

Table 1. Parameters defining the six constant pressure legs. Leg names A – G are as in Figure 1. Time intervals (in min) correspond to each leg in Figure 2, counting from the beginning of leg A.

The comparison between ALIMA data (resolution 0.9 km) and ECMWF IFS reanalysis on 12 September 00UTC is shown in Figure 3. It shows T as a function of altitude and time as retrieved from ALIMA during the full flight. The observed general variability mimics the latitude sectors and synoptic conditions cut across by HALO. The ALIMA T profile at 00UTC exhibits an intense wave structure up to the mesopause (Figure 3b). A relative agreement is observed in the stratosphere. The model progressively fails to solve the wavelike structure above 55 km. Note that experimental vertical profiles of horizontal or vertical wind are not available from this campaign.

a)

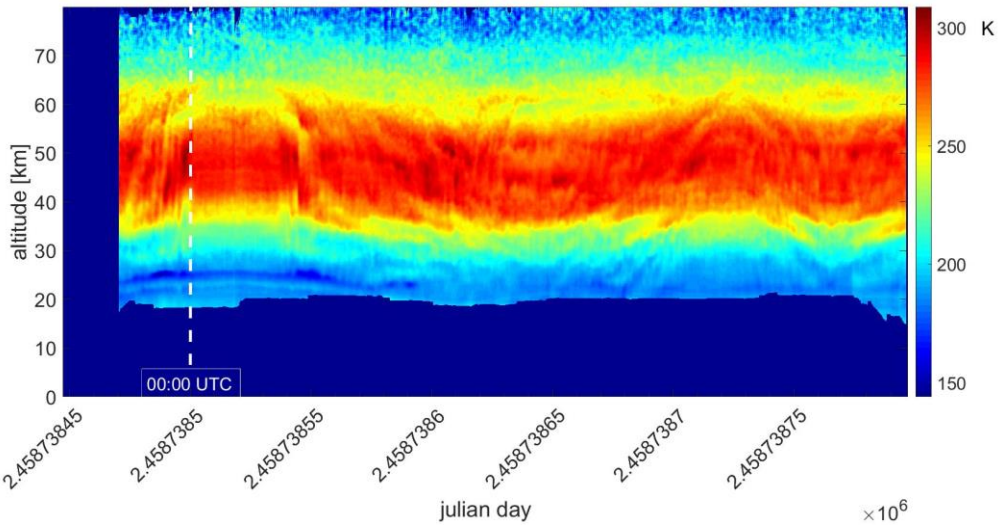

b)

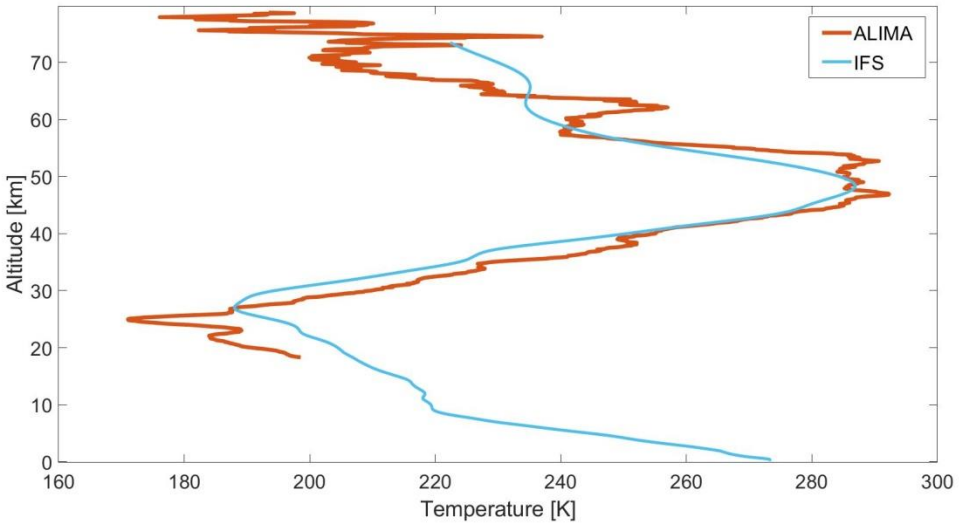

Figure 3. (a) Time-altitude section of temperature retrieved by the ALIMA lidar during flight ST08 along the flight track covering different regions and containng sharp turns as shown in Fig. 2. The dashed white line marks 0 UT on September 2019 when HALO crossed the highest peak of the southern Andes at 50.01 S and 74.97 E and for which we use IFS reanalysis. (b) IFS and ALIMA T for this time are compared.

Figure 4a show the IFS u', v' and T' residuals at the 00UTC HALO position at 50.01 S and 73.97 E. A highpass runing mean filter was applied to keep vertical wavelengths below a cutoff of 15 km in order to retain in the profiles mainly GWs, filtering out possible and non negligible planetary wave and tide contributions. A general more intense GW activity is observed in the strato-mesosphere regions compared to lower levels. Note the large amplitude oscillation in the selected vertical interval. Despite partially exceeding our imposed limit where the sponge begins at 55 km, the vertical interval between 43.0 and 66.5 km allows to illustrate the classic hodographic method. In Figure 4b, an anticlockwise rotation of the horizontal velocity perturbation with increasing altitude is observed in the selected interval. This indicates a dominant upgoing and probably non-orographic inertia GWpossibly generated close to jet levels, where the GW amplitude was observed to be considerably smaller.

a)

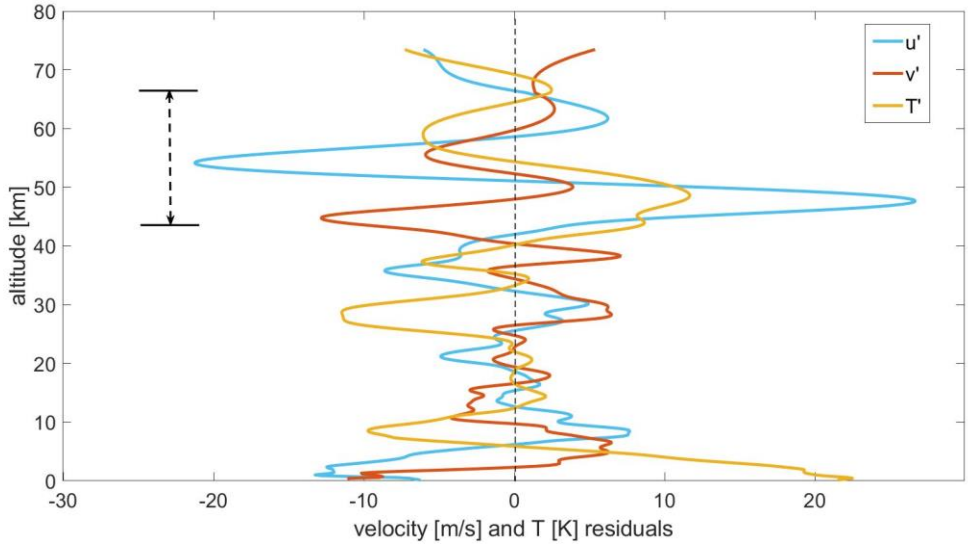

b)

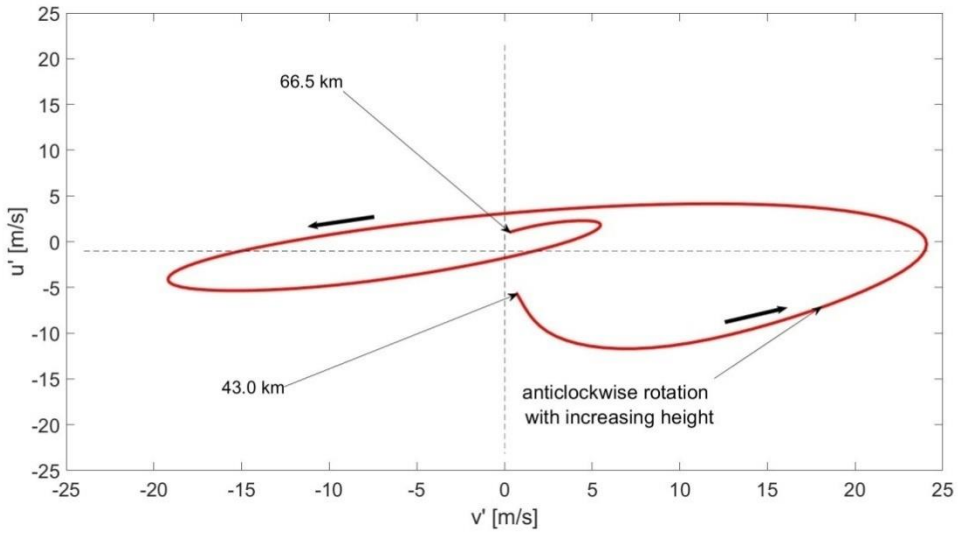

Figure 4. a) Zonal and meridional wind and temperature residuals at 00UTC HALO position (latitude/longitude = -50.01/-73.97), during ST08 flight on September 12, 2019. A highpass filter for vertical wavelengths below 15 km was applied. A selected highlighted vertical interval (43.0-66.5 km) is shown. b) Hodograph corresponding to the vertical interval highlighted in a), showing the anticlockwise rotation with increasing height.

From IFS simulations, the detected average coldest height is situated at ~25 km (26 hPa). Here, the lapse rate changes sign (also in conjunction with the position of the polar night jet core -see next section-). Then we divide the overall altitude interval below the IFS sponge layer into two sectors: [0, 25] km and [25, 55] km, namely, lower and upper height intervals (LHI and UHI),

respectively. Figure 5 illustrates vertical T profiles from IFS data, at an arbitrary longitude (70°W), every 5° between 45°S and 80°S. The profiles exhibit typical lapse rates above and below the ACH in the region considered in this study. The ACH is substantially higher than the average thermal tropopause, according to the frequent multiple tropopauses structure.

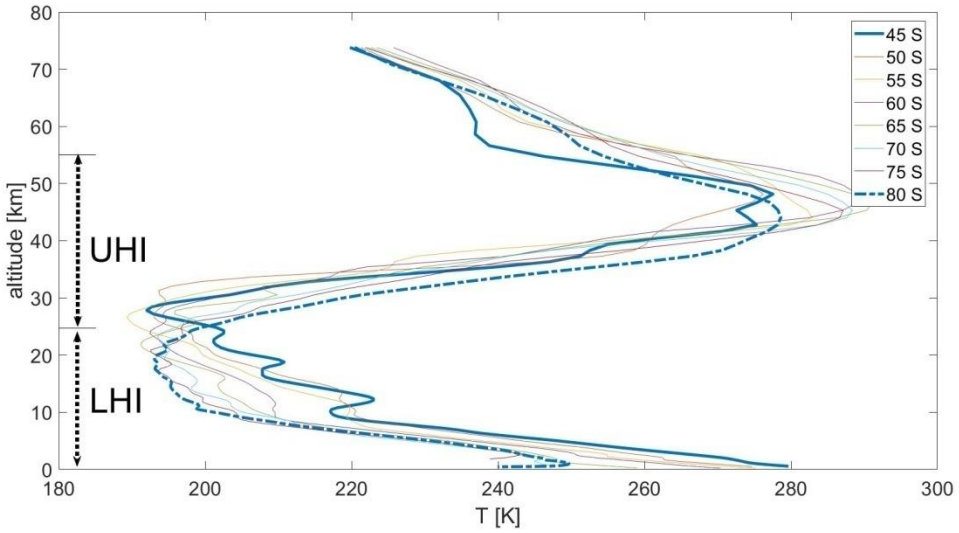

Figure 5. Vertical T profiles from IFS data at 70°W, every 5° between 45°S and 80°S, exhibiting the typical lapse rates above and below the ACH in the region considered in this study.

4 SRA at 00UTC on September 12, 2019

4.1 LHI (Lower Height Interval)

After an interpolation in log-pressure vertical coordinates, a Hanning taper to reduce the spectral leakage is applied to u' and v'. Following the spectral transformation described in section 2 (eq. (4) to (10)) C_R, E_T and NC_R are obtained in the position HALO was at 00UTC, 12 September (flight 08). An altitude column between 0 and 25 km is considered here.C_R (see Figure 6), E_T (= S_-+ S_+) and NC_R (not shown) exhibit relevant amplitudes only at the first harmonics.

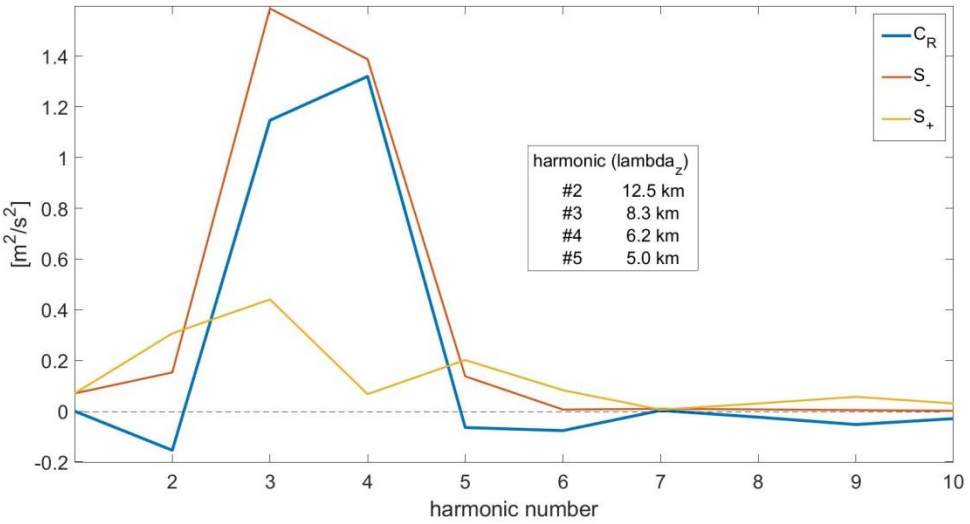

Figure 6. Rotary, counterclockwise and clockwise energy coefficient (C_R, S_- and S_+, respectively) corresponding to the first 10 harmonics obtained in LHI (between 0 and 25 km height), at the 00UTC HALO position (lat/lon= -50.01/-73.97) on September 12, 2019, during ST08 flight.

Significant rotational energy is distributed between harmonics #2 and #5, which correspond to vertical wavelengths(λ_z) between 12.5 and 5 km, revealing a clear dominant net upwards flux. For harmonics larger than #5 (λ_z< 5.0 km), the remaining rotational energy suddenly decreases to negligible values. The HALO flight position at the lat/lon pixel corresponding to this figure lies immediately west of the mountains, not strictly above them. Accordingly, modes with C_R different from 0 (not LP) suggest a significant GW contribution possibly originated in non-orographic sources. We may wonder under what conditions the GW energy at any pixel can be adequately described by only a few modes. The concept of a possible dominant quasi-monochromatic GW packet at any geographical position seems questionable, at least in the complex region considered here.

We extend the analysis illustrated in a single column (pixel) to the overall latitude-longitude region, made up by 1001x351=351,351 independent (0.1°x0.1°) pixels. In doing so, we delimit our geographic area of interest: [45S-80S, 120E-20E].

We define, for each harmonic, two quantities:

1) The total rotary coefficient, $TC_R^{(i)}(m)$, equal to the sum of $C_R(m)$ over all the p_i-pixels. Here, i = (a) anticlockwise, (lp) linearly polarized or (c) clockwise and $p_a(m) + p_n(m) + p_c(m) = 351{,}351$

pixels, for each m. $TC_R^{(i)}(m)$ may be interpreted as the total up- and downgoingGW energy, as a function of each vertical wavelength.

2) The average rotary coefficient, $AC_R^{(i)}(m) = TC_R^{(i)}(m) / p_i(m)$, that is to say, $TC_R^{(i)}(m)$ normalized over the total number of p_i-pixels. $AC_R^{(i)}(m)$ may be interpreted as the distribution of GW energy density at each p_i subsector, within the overall geographic domain. For example, we expect to observe enhanced upgoingGW energy flux concentrated around mountain areas. If we select any different geographic region, this will modify both $TC_R^{(i)}(m)$ and $AC_R^{(i)}(m)$.

According to the criteria we use to distinguish between orographic from non-orographic GWs, those pixels with $C_R(m)$ lying close to 0 are identified as LP. The "closeness" of $C_R(m)$ to 0 for a given m is, of course, arbitrary. To isolate LP GWs, we may choose, for example, upper and lower C_R thresholds as $[-\alpha, +\alpha]$ m^2/s^2, where $0 < \alpha << 1$. However, GWs from orographic origin are expected to be LP and, in addition, upgoing. Then, we propose that C_R must be > 0 and we set the upper and lower thresholds: $[0, +\alpha]$ m^2/s^2. To illustrate the variability arising from these constraints, in Figure 7 we show $TC_R^{(i)}(m)$ for the first 15 harmonics and three arbitrary upper thresholds: α = 0.1, 0.2 and 0.3.

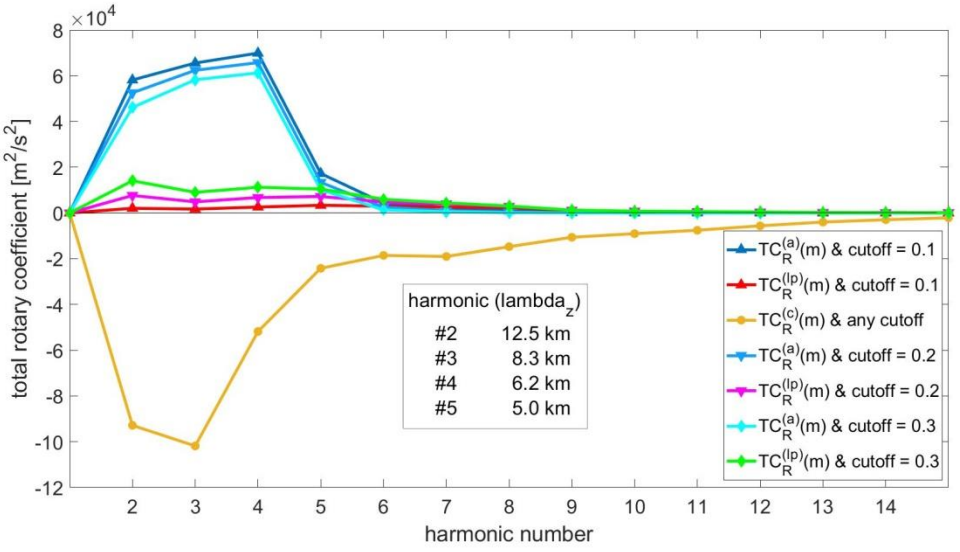

Figure 7. Total rotary coefficient, $TC_R^{(i)}$, calculated in the overall latitude-longitude region, made up by 1001x351=351,351 (0.1°x0.1°) pixels. i = (a) anticlockwise, (lp) linearly polarized or (c) clockwise GW rotation. Three cutoffs defined to distinguish between GWs of orographic and non orographic sources are arbitrarily chosen to show the variability of each upgoing contribution to the overall energy flux. According to our definition, different upper cutoffs do not affect downgoing GWs.

385 Some features may be noted:

386 • The main energy flux is concentrated in the lower harmonics. A fast decrease in $TC_R^{(a)}$
387 with increasing m reveals an accumulation of GW energy only in this spectral range. A
388 net larger downgoing energy flux is observed above the overall geographic sector
389 considered here. At first glance, this result may be somehow unanticipated, if we do not
390 take into account that most of the region is covered by oceanic areas, in comparison to
391 mountain regions.
392 • $TC_R^{(c)}$ corresponding to downgoing GW rotational energy flux, in turn, diminishes with m
393 considerably slower. This energy is spread into additional shorter vertical wavelengths
394 than $TC_R^{(a)}$. It is unaffected by the variability in the upper cutoff.
395 • Downwards GW energy flux distribution among larger m values suggest a possible
396 relevance of inertia GWs, generated after geostrophic imbalance close to or at polar night
397 jet levels. In addition, reflection effects may be significant.
398 • $TC_R^{(a)}$($TC_R^{(lp)}$) decreases(increases) with increasing(decreasing) upper cutoff. We remind
399 that these two parameters share the total available upgoing energy flux.

400 In Figure 8, we show the $AC_R^{(i)}$ distribution.

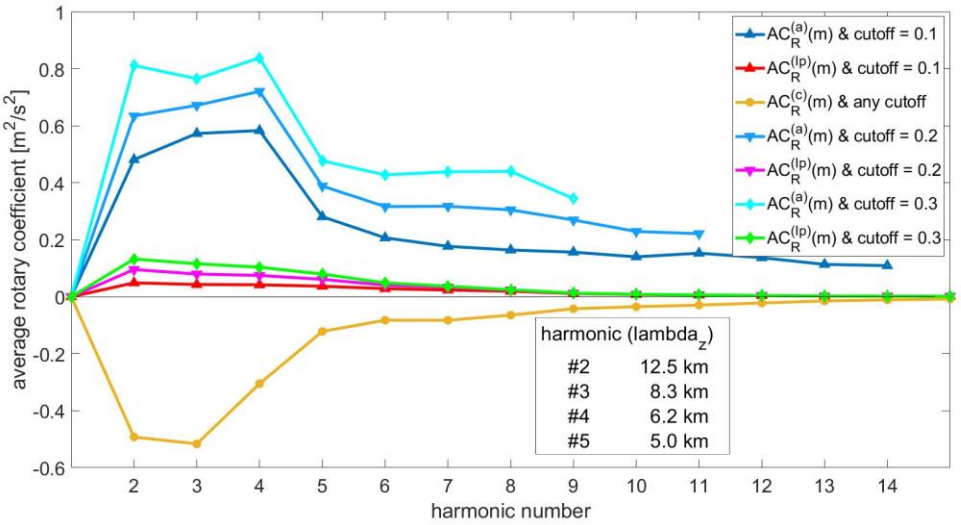

401

402 **Figure 8.** Average rotary coefficient, $AC_R^{(i)}$, calculated in the latitude-longitude region as in Figure 7.

403 The following features can be observed:

- The relative relevance of upgoing as compared to downgoing GW energy per unit area is now evident. Clearly, it is concentrated in limited subregions, mostly corresponding to mountain areas. These are defined by a considerably lower pixels number than those corresponding to downgoingGWs.
- $AC_R^{(a)}$ is here always larger than $AC_R^{(c)}$ and increases with increasing upper cutoff, inversely to what is observed when comparing $TC_R^{(a)}$ and $TC_R^{(c)}$. $AC_R^{(lp)}$ increases with increasing upper cutoff, similarly to what happens with $TC_R^{(lp)}$.
- As the cutoff is set to larger values, p_a is equal to zero beyond a given harmonic and $AC_R^{(a)}$ is obviously not defined. For these higher cutoffs, the total available upgoingGW energy flux seems to be shared only between a few harmonics.
- The enhance of $AC_R^{(lp)}$ with increasing cutoff, also observed in $TC_R^{(lp)}$, suggests that the number of pixels defining the total area with LP GWs seems not to expand significantly. These are are concentrated in reduced areas.

In Figure 9 we analyze the geographic distribution of $C_R(m)$, now in a latitude-longitude plot. For illustrative purposes, we first perform an approximation of the general characteristics that can be extracted from this parameter. We select one representative dominant harmonic (#3), based on the results in Figure 8. This harmonic corresponds to λ_Z = 8.3 km. The plot was obtained at 00UTC, on 12 September 2019.

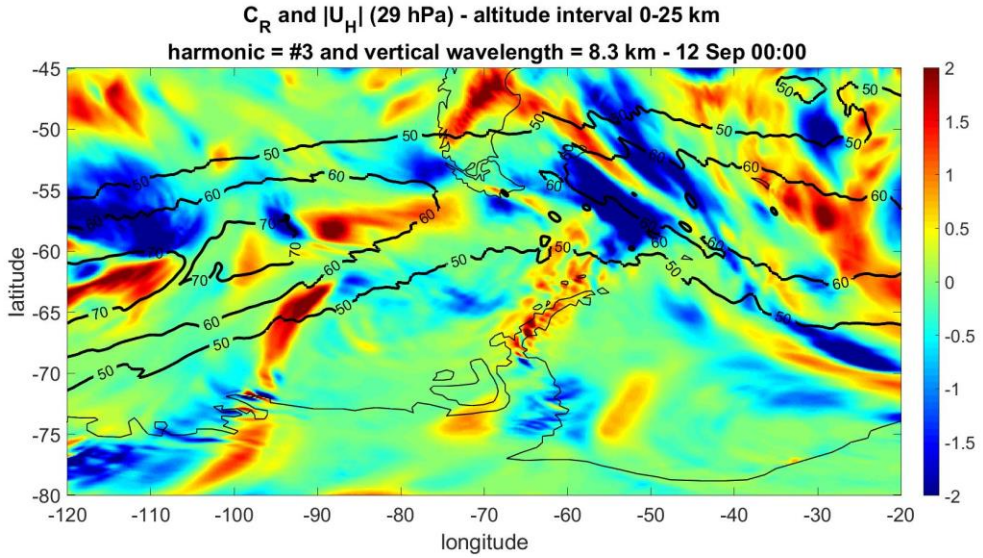

Figure 9. Rotary coefficient for harmonic #3 in [m^2/s^2], corresponding to λ_Z = 8.3 km. The black isolines show the absolute value of the horizontal wind in [m/s] at 29 hPa, where the core of the polar night jet is found.

We interpret the different pixel regions as follows. Positive(negative) C_R values correspond to GW packets with dominant anticlockwise(clockwise) rotation with increasing height. This is what is expected from upwards(downwards) energy propagation in the southern hemisphere. Pixels with C_R bounded between 0 and α with $\alpha << 1$ indicate subregions where one of two possible characteristics prevails: dominant LP, as expected from typical MWs (as explained before, we consider only $\alpha > 0$), or with negligible GW activity. This uncertainty may be removed by plotting E_T (m) for the same #3 harmonic (see below). The position of the jet core (black contours) is situated above oceanic and continental areas at 25 km height (26 hPa). Some features can be identified from this figure, bearing in mind that it corresponds only to a single harmonic:

- Two subregions with upwards propagating GW energy above continental areas over central Patagonia and the Antarctic Peninsula show different degrees of elliptic polarization.
- Above southern Patagonia and Tierra del Fuego Island, there is a predominance of LP GWs, suggesting their orographic origin.
- Above the remaining oceanic areas, there is a broad distribution of up- and downgoing energy flux. In particular, at and near to the jet and the jet streak position. As mentioned before, possible sources for this variability may be found in departures from geostrophic equilibrium near to the jet and the proximity to the cold front.

In Figure 10 we show E_T ,also for #3:

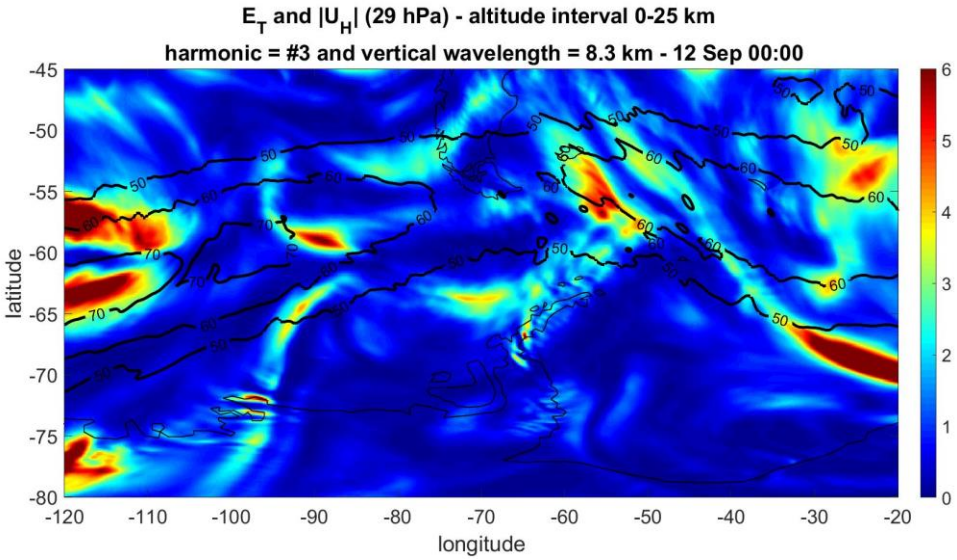

Figure 10. Total rotary energy for harmonic #3 in [m^2/s^2], corresponding to λ_Z = 8.3 km. The black isolines show the absolute value of the horizontal wind in [m/s] at 29 hPa, where the core of the polar night jet is found.

The following features are observed:

- A geographic correspondence between subregions where E_T is enhanced and extreme C_R values (Figure 9). This is seen mostly near to the jet (Figure 10).
- This feature also applies to central Patagonia and the Antarctic Peninsula, although with less intense E_T values than near the jet stream. Taking into account that the characteristics observed in figures 9 and 10 are very different for any different m, in videos 1 and 2 we extend the description of figures 9 and 10 respectively,as a function of m between #2 and #6. The distributions of C_R and E_T are shown. Equal scales were preserved within each video, for comparison. There is a general increasing variability with increasing m of the up- and downgoing structures. This provides an insight of the complex GW ensemble to be expected in the region considered here.
- The geographic distribution of the enhanced $C_R$subregions is different for each harmonic. The same is observed for subregions where LP GWs are expected.
- The opportunity of isolating geographic sub-regions where monochromatic waves would dominate seems unrealistic.
- The overall amplitude of C_R decreases with increasing m, as expected from the features in Figure 7.

- As in the case of C_R, the geographical distribution of sub-regions of enhanced E_T is different for each m. An overall decrease in E_T with increasing m is also evident. To better appreciate the cumulative effect through m of C_R and E_T, in Figures 11 and 12 these parameters are addedover the whole set of harmonics, namely, $C_{R\,(INT)}$ and $E_{T\,(INT)}$, respectively. Note that these figures were rescaled with respect to Figures 9 and 10.

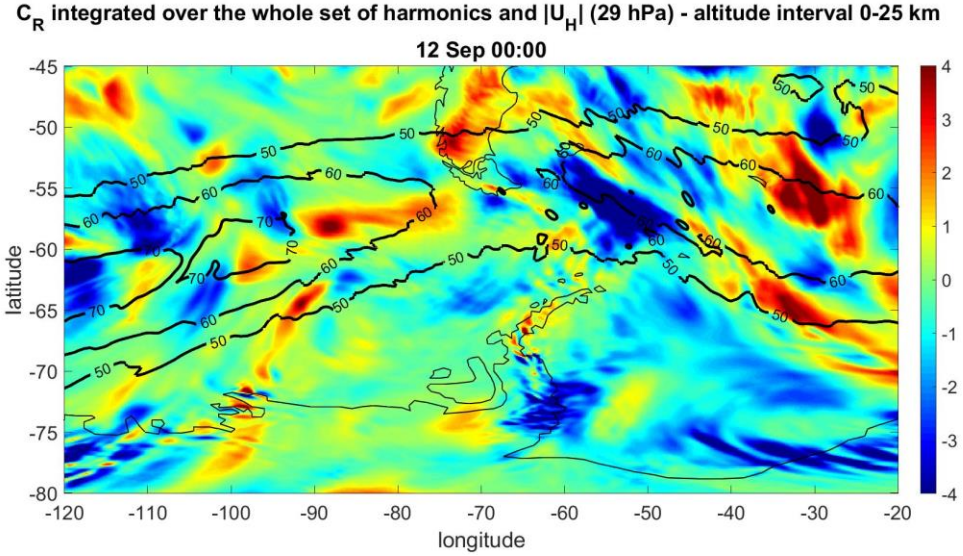

Figure 11. $C_{R\,(INT)}$, in [m^2/s^2], obtained by adding all the harmonics C_R (m).

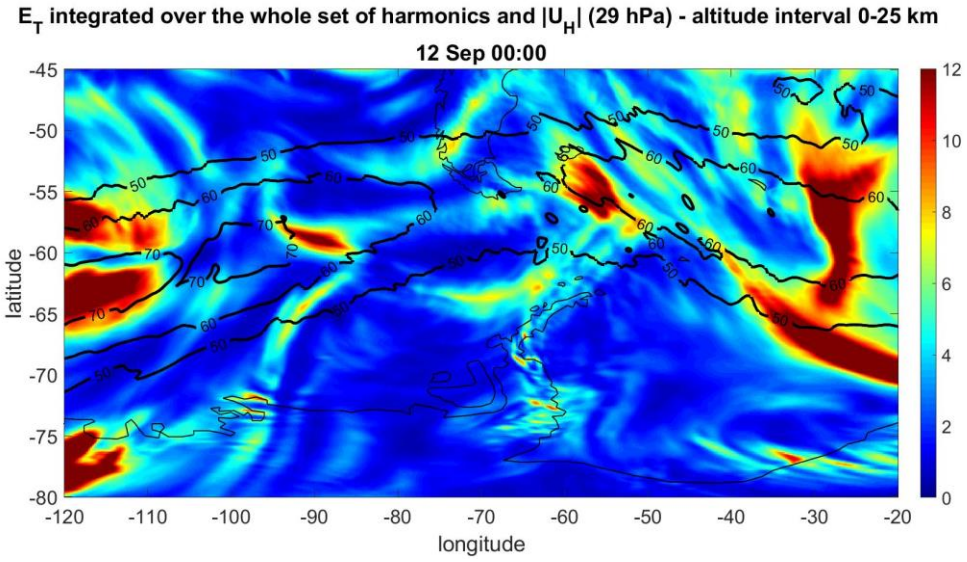

Figure 12. $E_{T\,(INT)}$, in [m^2/s^2], obtained by adding all the harmonics E_T (m).

In addition to the general characteristics already described, near the jet, a high concentration of GW energy with a significant degree of non-linear polarization is evident, especially over oceanic areas.

In Figure 13, we classify the distributions from Figures 11 and 12 in four groups as follows: GW packets with i) negligible total wave energy, ii) anticlockwise rotation, iii) mainly LP and iv) clockwise rotation.We label each of these 4 groups with an index "0", "1", "2" or "3" respectively. Sub-regions where the total wave energy remains below an arbitrarily cutoff C = 1 m^2/s^2 (group i), we assign an index “0”. If the energy is greater than C, we assign an index “1” or “3”, for C_R negative or positive, respectively. Finally, we assign “2” if C_R lies within the interval [0, +r] (after Figures 7 and 8, for brevity we only illustrate with r = 0.3 m^2/s^2). We interpret this last group as containing the dominant LP GW packets.

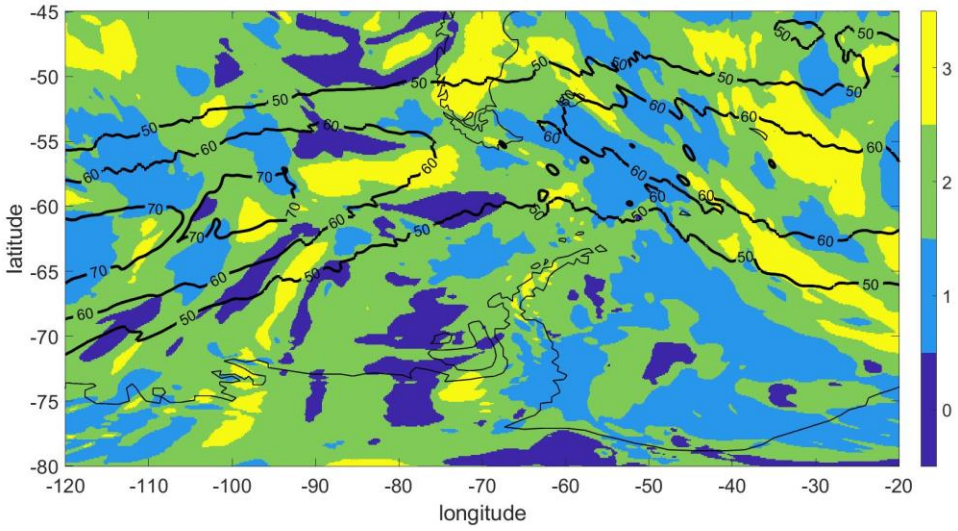

Figure 13. The four areas with different up- and downgoing dominated GWs. Labels “0”, “1”, “2” and “3”, indicate, respectively, C_R values with negligible total rotational energy, downgoing dominated GW energy flux, LP and upgoing. Here C = 1 m^2/s^2 and r = 0.3 m^2/s^2.

The following features may be noted:

- UpgoingGW energy flux subregions (“3”) (or pixel groups) are mostly situated above Patagonia, Antarctic Peninsula and several oceanic sectors. The latter alternate with subregions dominated by LP GWs (“2”).

- The downstream GW sectors ("1") only appear above the sea. As mentioned above, they represent the main contribution in terms of relative areas (but not in terms of relative energy flux contribution, as explained after Figure 8) of the overall region under consideration.
- For any value of C, the relative coverage of zones "2" and "3" obviously still depends on r, although, the sum of the two remains unchanged. For example, if we set r = 0.1 (figure 8), region "2" will decrease considerably and "1" will increase. If C is modified, the relative distribution of the 4 regions will also change.

In video 3, we show the evolution through successive m values of the normalized rotary coefficient (NC_R). Clearly, the horizontal spatial scale of variability of this relative dimensionless coefficient, which is bounded by -1 and +1, considerably increases with m. The complex structure of the different wave packets becomes more evident here than in C_R and E_T. It must be remarked that the information available from the 3 coefficients, C_R, E_T and NC_R is, in some sense, complementary. For example, let us consider extreme values: if NC_R is 1 or -1 we do not know whether the upward or downward rotational energy flux is large or small. This knowledge is provided by C_R or E_T. On the other hand, if NC_R is close to 0, from C_R alone no information about E_T is available. However, in this case from NC_R we infer that the energy flux associated to the presumed LP mountain waves is significant. In video 3, this occurs in the transition zones between red and blue sectors. Nevertheless, it must be remarked that the conclusions drawn from each image are valid only for its corresponding harmonic.

4.2. UHI (Upper Height Interval)

Following the procedure applied in section 4.1, we now consider the interval [25, 55] km. Note that instead of the simple separation proposed here between LHI and UHI, other spectral intervals could also reveal significant features and possible sources, e.g. a sliding vertical window or non overlapping vertical intervals with different lengths. We expect that the coercive presence of the jet may provide a “turning point” in the net vertical energy flux. Regions where geostrophic unbalance exists near to the jet may constitute a non negligible GWs source. In the absence of critical layers, orographic GWs may also be able to propagate high in the stratosphere; hence, we expect that the two main sources of upgoing GWs are the same as in LHI. Figures 14 to 21 represent, respectively, the counterparts of Figures 6 to 13 in UHI.

On the basis of the description already made in the previous section, in UHI, the relevant similarities with and differences from the lower levels are detailed below each figure.

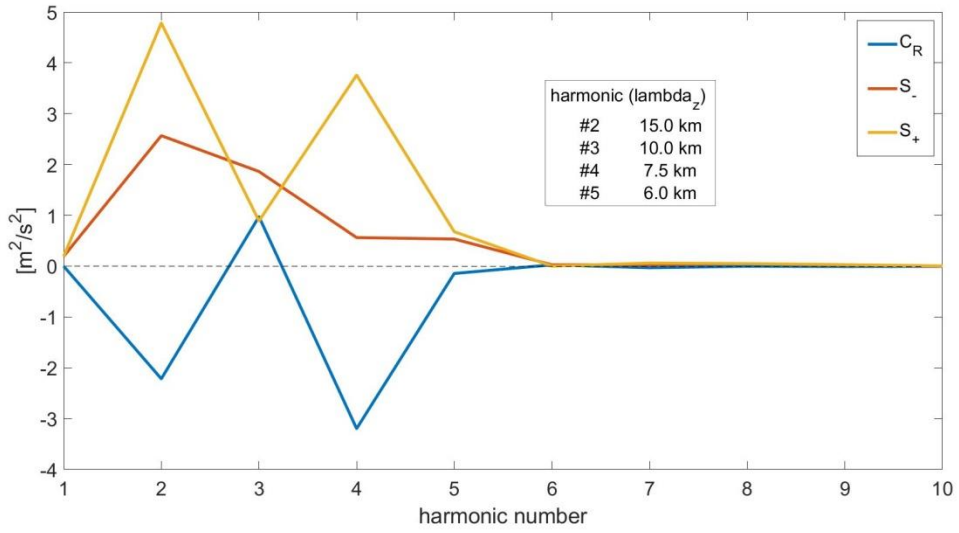

Figure 14. As in Figure 6, rotary, counterclockwise and clockwise energy coefficient corresponding to the first 10 harmonics obtained in UHI (between 25 and 55 km height), at the 00UTC HALO position.

In Figure 14, the significant rotational energy in UHI at the single pixel corresponding to the 00UTC HALO position (lat/lon = -50.01/-73.97) on September 12, 2019, during ST08 flight is shown. It is distributed within the first harmonics, mainly #2 and #4. These correspond to λ_z equal to 15.0 and 7.5 km, but, in UHI, they reveal a net downwards flux. For harmonics larger than #5, the remaining rotational energy decreases to negligible amplitudes. As in LHI, C_R different from 0, suggests that a significant GW contribution originated in non-orographic sources or that reflection occurred. For #3 (λ_z =10.0 km) C_R close to 0 may correspond to an orographic mode.

In Figure 15, identical remarks to those after Figure 7 can be made. The effect of only two arbitrary cutoffs in the energy flux distribution is shown for illustration.

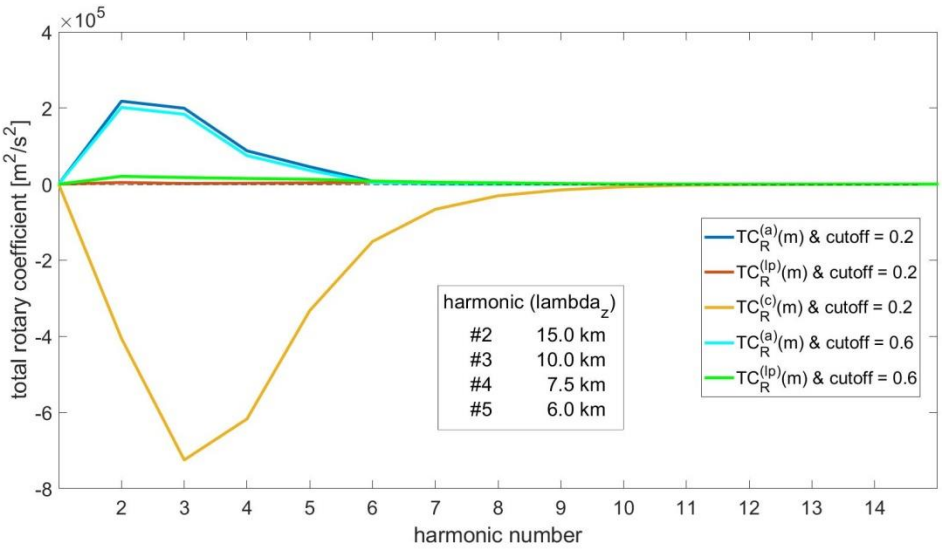

Figure 15. As in Figure 7, $TC_R^{(i)}$ is shown in the overall latitude-longitude region, between 25 and 55 km height. Here, the effect of two cutoffs is shown.

In Figure 16, we now show the $AC_R^{(i)}$ distribution. It can be observed that, contrary to what happens in LHI, the average upgoing GW energy flux is weaker than the downgoing flux, even though it is probably concentrated in limited mountainous regions.

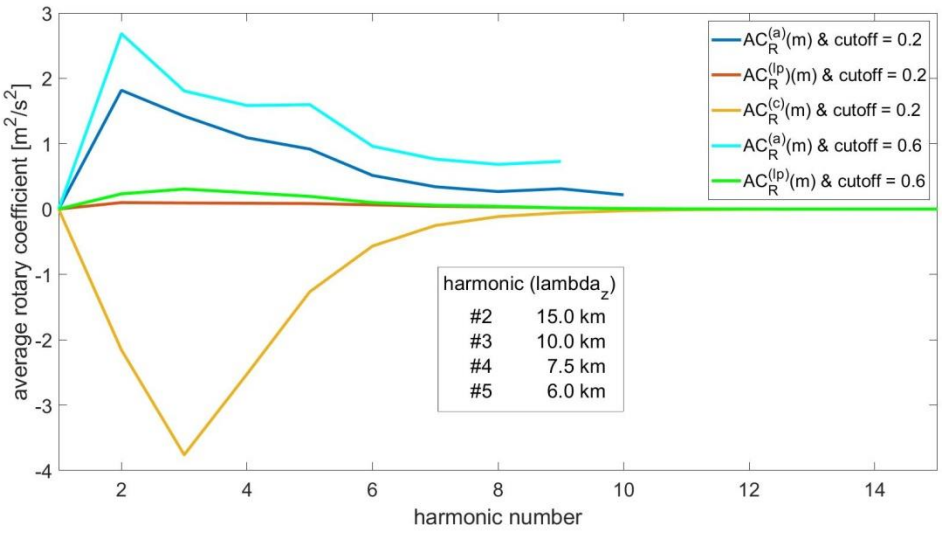

Figure 16. Average rotary coefficient, $AC_R^{(i)}$, calculated in the latitude-longitude region as before. The effect of two cutoffs is shown.

548 In Figure 17, we analyze the geographic distribution of C_R(m) in a latitude-longitude plot,
549 selecting one representative dominant harmonic (#3), as in Figure 9. This harmonic corresponds
550 to λ_Z equal to 8.3 km. The plot was rescaled, taking into account that C_R (and E_T below in Figure
551 18) are in units of energy per unit mass. These magnitudes are expected to increase in the
552 stratospheric altitudes due to the decrease in air density.

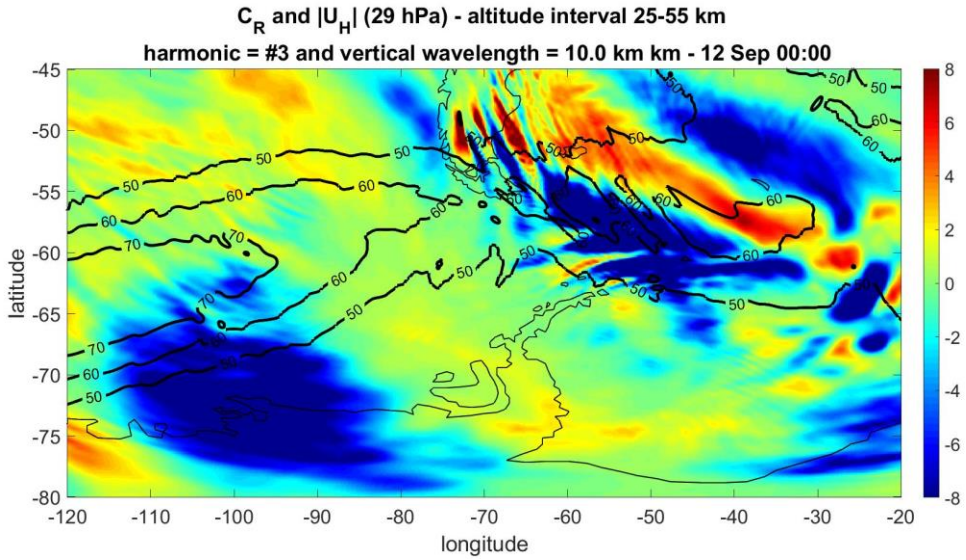

553

554 **Figure 17.** Rotary coefficient for harmonic #3 in [m^2/s^2], corresponding to λ_Z = 10.0 km. The black isolines show
555 the absolute value of the horizontal wind in [m/s] at 29 hPa, where the core of the polar night jet is found.

556 Following the general considerations stated above for Figure 9, we interpret the different regions
557 in Figure 17 as follows: positive(negative) C_R values correspond to GW packets with dominant
558 anticlockwise(clockwise) rotation with increasing height. This is what is expected from
559 upwards(downwards) energy propagation in the southern hemisphere. Pixels with $0 < C_R < \alpha \ll 1$
560 indicate subregions where one of two possible characteristics prevails: dominant LP, as expected
561 from typical MWs (as explained before, we consider only $\alpha > 0$), or with negligible GW activity.
562 This uncertainty may be removed by plotting E_T (m) for the same #3 harmonic (Figure 18). The
563 position of the jet core (black contours) is situated above oceanic and continental areas at 25 km
564 height (26 hPa). From this figure:

565 • Two subregions with upwards propagating GW energy above continental areas of central
566 Patagonia and the Antarctic Peninsula, showing different degrees of elliptic polarization.

- Above southern Patagonia and Tierra del Fuego Island, a predominance of LP GWs is clear, suggesting an orographic origin.
- Above the remaining oceanic areas, there is a broad distribution of up- and downgoing energy flux, in particular at and near to the jet and the jet streak position. As mentioned before, possible sources for this variability may be found in departures from geostrophic equilibrium near to the jet.

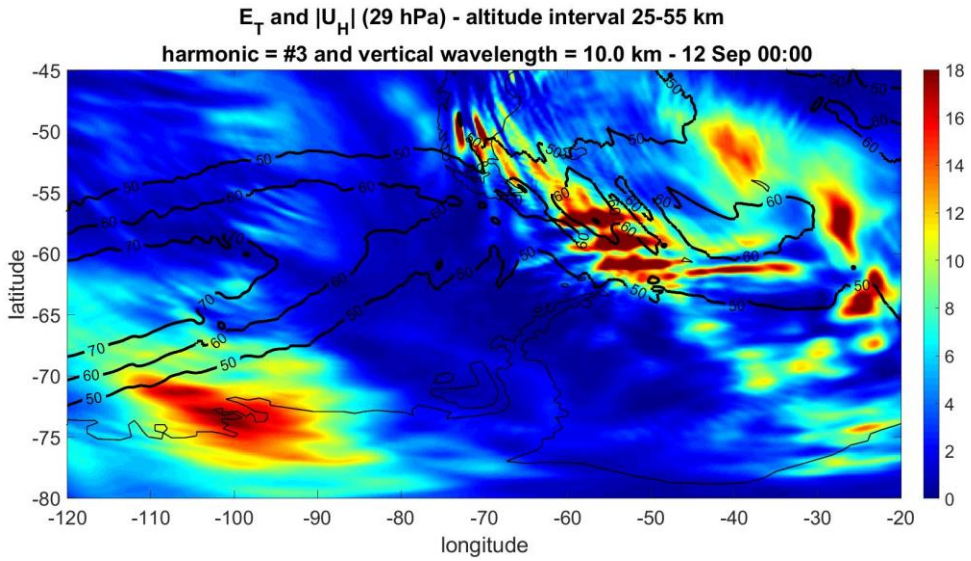

Figure 18. Total rotary energy for harmonic #3 in [m^2/s^2], corresponding to λ_Z = 10.0 km. The black isolines show the absolute value of the horizontal wind in [m/s] at 29 hPa, where the core of the polar night jet is found.

The cumulative effect through m, of C_R and E_T in UHI ($C_{R\,(INT)}$ and $E_{T\,(INT)}$) is shown in Figures 19 and 20. The regions where upward and downward flows with significant departures from linear polarization are observed to the east of 70W meridian and in the South Pacific.This is also observed in E_T.

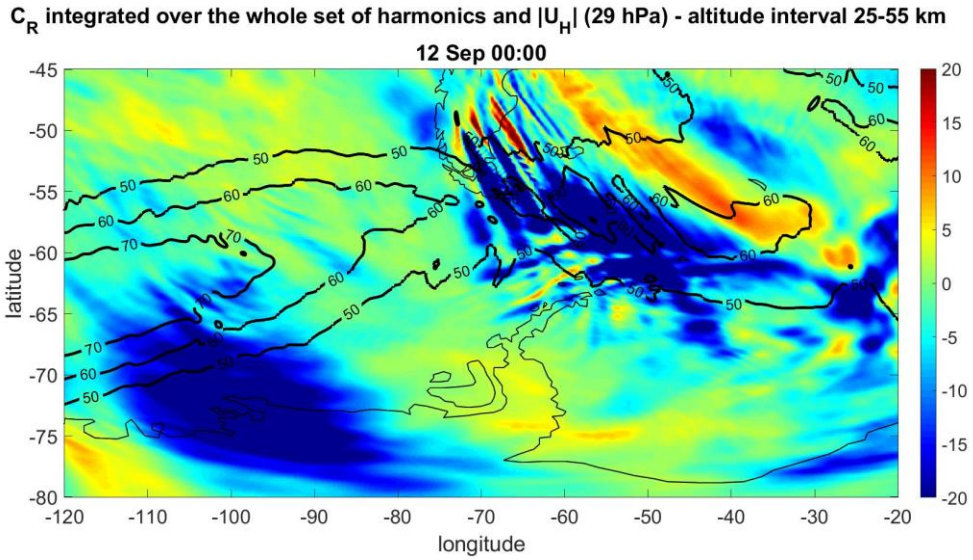

581

582 **Figure 19.** $C_{R\,(INT)}$, in [m^2/s^2], obtained by adding all the harmonics C_R (m).

583 In Figure 20,it may be observed that in UHI, the total available GW energy per unit mass is, on
584 average, around five times larger than in LHI.

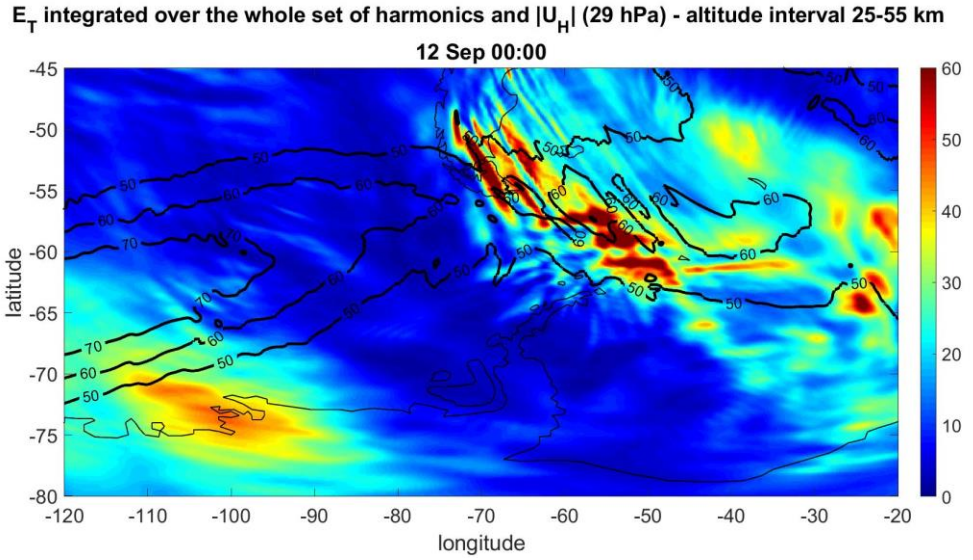

585

586 **Figure 20.** $E_{T\,(INT)}$, in [m^2/s^2], obtained by adding all the harmonics E_T (m).

587 In Figure 21, thresholds C = 10.0 m^2/s^2 and r = 4.0 m^2/s^2 are adapted to the energy distribution
588 now observed in UHI.

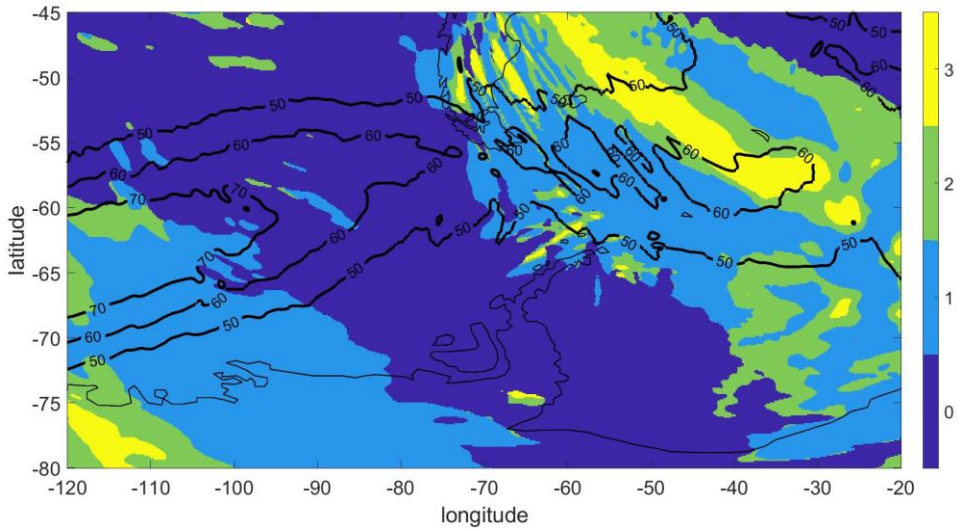

589

590 **Figure 21.** As in Figure 13, the four areas with different up- and downgoing dominated GWs. Labels "0", "1", "2"
591 and "3", indicate, respectively, C_R values with negligible total rotational energy, downgoing dominated GW energy
592 flux, LP and upgoing. Here C = 10.0 m^2/s^2 and r = 4.0 m^2/s^2.

593 We can observe sub-regions with different degrees of polarization where downward flows
594 dominate, systematically distributed in elongated bands. These are of different widths and have a
595 predominantly NW-SE direction. Their relative distribution depends, as in LHI, on the arbitrary
596 choice of r and C cutoffs.

597 Finally, for completeness, we include videos 4 to 6, which are respectively UHI counterparts of
598 videos 1 to 3. We recall that the characteristics and conclusions drawn from each image shown in
599 each of the videos 1 to 6 are valid only for the corresponding harmonic and are notably different
600 for the rest of the harmonics.

601 **5 A comparison with a GW temperature-vertical wind phase difference based analysis**

602 We corroborate our rotational analysis with an independent technique that also allows us to
603 investigate the upward or downward direction of wave energy propagation. This alternative
604 analysis was based on the same ECMWF IFS operational analysis data for 12 September 2019,
605 00:00 UTC, as the rotational analysis introduced above. A brief description of the alternative
606 technique is given below.

607 ECMWF data was processed using small-volume few-wave decomposition method S3D
608 (Lehmann et al., 2012), currently implemented as part of the JUWAVE package for GW analysis

developed in ForschungszentrumJülich. S3D uses least-squares fitting to determine the amplitude, 3-D wave vector and phase of several highest amplitude waves in a relatively small rectangular box (boxes measured 300 km by 300 km in horizontal and 6 km in the vertical direction in this study). S3D was used to independently find waves (harmonic disturbances) in temperature and vertical wind data. If both temperature and wind disturbances were indeed a consequence of GW activity, their phases and amplitudes must satisfy certain conditions that can be derived from linear GW theory. Following, for example, Section 2.1 of Fritts & Alexander (2003), one can describe GWs as linear disturbances on a hydrostatic main state satisfying WKB (Gill, 1982) conditions. Temperature and vertical wind disturbances with amplitudes and phases T_A, Φ_T and w_A, Φ_w can then be written as

$$T = T_A e^{z/2H} \cos(kx + ly + zm - \omega t + \Phi_T) \quad (11)$$

$$w = w_A e^{z/2H} \cos(kx + ly + zm - \omega t + \Phi_w) \quad (12)$$

where (k, l, m) is the 3-D wave vector, t is time, ω is the wave frequency and H is the scale height. We also assume that speed of sound is very large, to eliminate acoustic waves from the analysis. Then, it follows from equation (18) in Fritts & Alexander that $\Phi_T - \Phi_w$ is $\pi/2$ for upward propagating waves, $-\pi/2$ for downward propagating waves and

$$\frac{T_A}{w_A} = \frac{T_0 N^2}{g\omega} \quad (13)$$

where T_0 is the undisturbed air temperature, N is the Brunt-Väisälä frequency, g is gravitational acceleration and ω is the intrinsic frequency of the wave (it can be obtained from the GW polarization relations knowing k, l, m from wave fit). These relations were used to determine whether each S3D fitting box contained GWs and whether they were propagating upwards or downwards. In particular, box was said to contain a GW if either $|\Phi_T - \Phi_w - \pi/2| < 0.2$ (upward propagating wave) or $|\Phi_T - \Phi_w + \pi/2| < 0.2$ (downward propagating wave) and

$$\frac{T_0 N^2}{2g\omega} < \frac{T_A}{w_A} < 2\frac{T_0 N^2}{g\omega} \quad (14)$$

i.e. T_A / w_A was between half and twice the theoretically predicted value.

S3D wave fits are most reliable when horizontal and vertical wavelengths of the detected wave are between about one third of the fitting box size and three fitting box sizes in the respective direction. Therefore, we only considered GWs with horizontal wavelengths between 100 km and 900 km and vertical wavelengths from 2 km to 18 km.

To compare this method to rotational analysis, gravity wave activity in a relatively large altitude range (LHI and UHI intervals) has to be quantified. It is evident from equations (11) and (12) that the amplitudes T_A and w_A grow exponentially with altitude. Hence, calculating mean amplitudes over a tall vertical column would almost entirely represent wave activity at the top of the column. To avoid this problem, we will quantify the amount of wave activity using the density of flux of the horizontal momentum (gravity wave momentum flux; GWMF)

$$F = \frac{\rho g^2(k,l)}{2mN^2}\left(\frac{T_A}{T_0}\right)^2 \quad (15)$$

whereρ is air density. This quantity is conserved as a wave propagates to higher altitudes (Ern et al., 2015), and hence mean |F| over a vertical column adequately describes the amount of wave activity over the entire column.

The results are presented in Figures 22 and 23. For greater data reliability, heavily overlapping S3D boxes were used. Each box measures 300 km by 300 km by 6 km, while box centers lie on a rectangular grid with 0.5 km spacing in the vertical, 0.2° spacing in the meridional direction and 0.3° spacing in the zonal direction. To produce Figures 22 and 23, mean |F| for each vertical column of boxes was first computed. Then, every grid point in the Figures was assigned a 300 km by 300 km square centered at that point. |F| value for this point was then computed as a mean of all vertical profiles with footprints overlapping the square, weighted by the area of the overlap.

A comparison of, for example, Figure 11 against Figures 23 and 23 reveals generally similar results in the most important regions considered here: upward propagating GWs dominate over the South America and Antarctic Peninsula, while areas with more downward propagation can be found over the Atlantic.

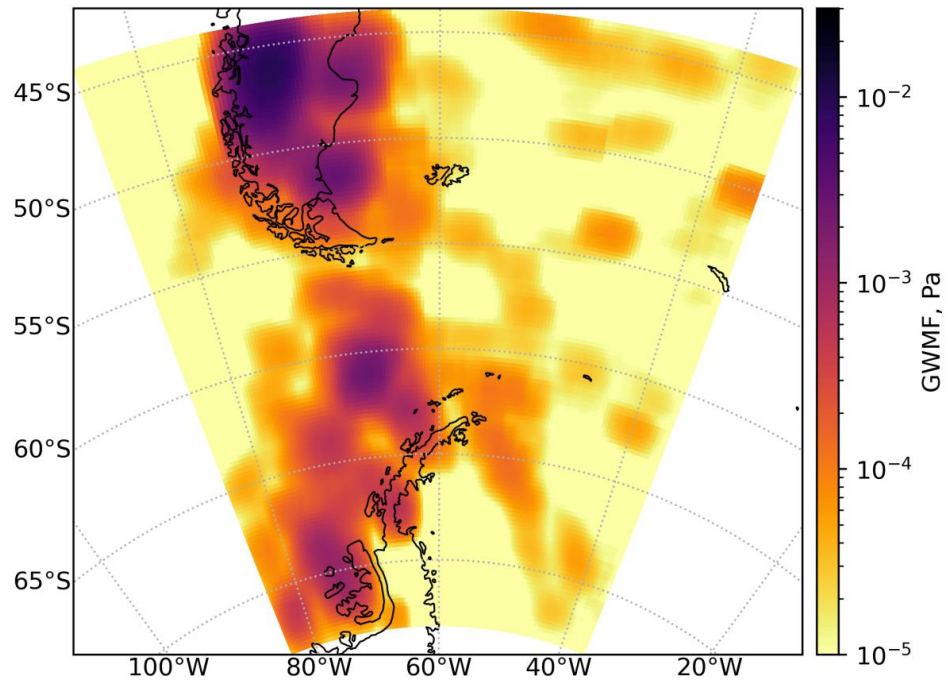

660

661 **Figure 22.** Mean gravity wave momentum flux of upward propagating waves, in the altitude
662 range from 3 km to 24 km.

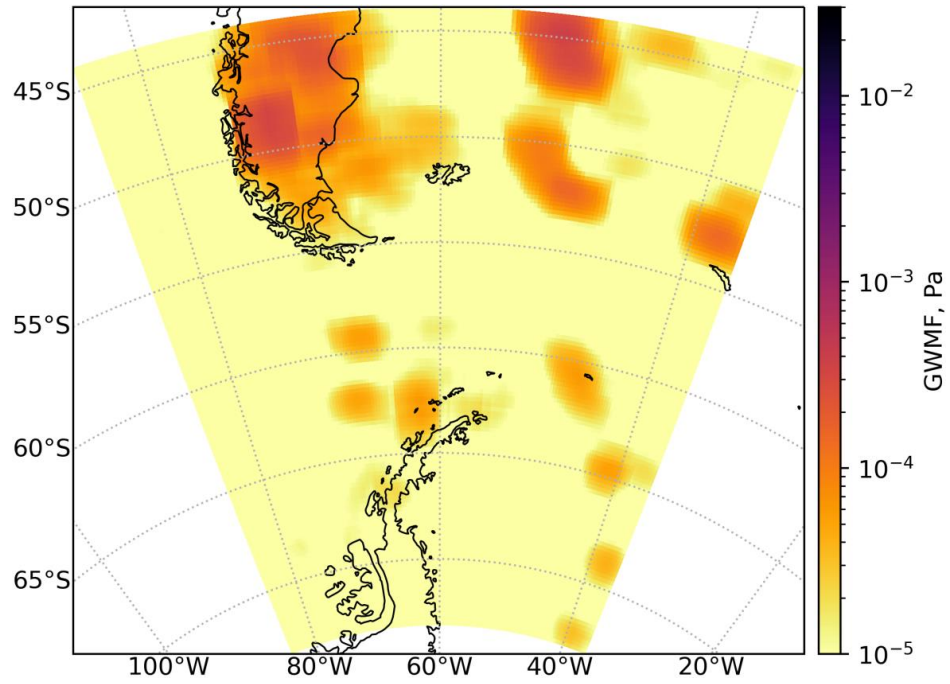

663

664 **Figure 23.** Mean gravity wave momentum flux of downward propagating waves, in the altitude
665 range from 3 km to 24 km.

It is worth recalling that a few years ago, in a study of GWs over Antarctica, Hertzog et al. (2008) observed, from long-duration superpressure balloon flights at stratospheric levels, mountain waves accounting for about two thirds of the total momentum flux. They found zonally averaged fluxes over the ocean similar in magnitude to those above the continent, underlining the importance of non-orographic GWs in the Southern Hemisphere polar and subpolar latitudes.

6 Conclusions

Based on IFS simulations, a rotary spectral, semi-quantitative classification of GWs is proposed according to their sources: orographic or non-orographic. Their degree of polarization is the main factor taken into account, from non-hydrostatic, non-rotating hydrostatic to rotating GWs, following their intrinsic frequency regimes. An alternative analysis may be to look at the time dependence (standing or non-stationary waves). This option can be performed on the basis of mesoscale simulations and is left for a future contribution.

In the extremely complex scenario of upward and downward GW packets found during one of the SOUTHTAC flights (Flight 08) above the southern Andes, Patagonia, the Antarctic Peninsula and the surrounding oceanic areas, the rotary-vector analysis method was applied. It is based on the Fourier transformation of a complex vector consisting in the perturbations to zonal and meridional wind components with vertical wavelengths less or equal than 15 km. It should be stressed that low frequency GWs are not exactly circularly polarized, except near the inertia frequency, and that even a purely upward or downward wave contributes to both the clockwise and counter-clockwise spectrum. In this sense, this analysis should be considered useful in a statistical sense. Moreover, based on its polarization nature alone, an identification of its likely sources can be made.

After a comparison between IFS simulations and lidar data obtained during one of the flights performed during the Southtrac Experiment, the region under study was divided into 2 disjoint vertical intervals. Here, the expected relevance of the polar night jet core in the radiation of GWs was taken into account.

In the lower height interval, the main energy flux is concentrated in the lower harmonics. A net larger downgoing energy flux is observed above the overall geographic sector, taking into account that most of it is covered by oceanic areas. Downward GW energy flux suggests the

possible relative relevance of inertia GWs, generated after geostrophic imbalance close to or at polar night jet levels and/or in the presence of a front. Instead, if we compute upward GW energy flux per unit area, this is larger than the downward one, because it is concentrated in limited sub-regions, mostly corresponding to mountain areas. In general, upgoing GW energy flux sub-regions are mostly situated above Patagonia, Antarctic Peninsula and several oceanic sectors where other sources like convection or frontal regions may be relevant enough. The latter alternate with sub-regions dominated by LP GWs. Downstream GW sectors only appear above the sea. As mentioned above, they represent the main contribution in terms of relative areas, but not in terms of relative energy flux contribution of the overall region. The relative coverage of upgoing zones with different degrees of polarization strongly depends on the two thresholds proposed in this paper.

In particular, by illustrating the GW activity for harmonic #3, which corresponds to a vertical wavelength of 8.3 km, two sub-regions with upwards propagating GW energy above continental areas in central Patagonia and the Antarctic Peninsula show different degrees of elliptic polarization. Above southern Patagonia and Tierra del Fuego Island, there is a predominance of LP GWs, suggesting their orographic origin. Above the remaining oceanic areas, there is a broad distribution of intense up- and downward energy flux, in particular, at and near to the jet and the jet streak position. As mentioned before, possible sources for this variability may be found in departures from geostrophic equilibrium near to the jet. We summarize the dominant GWs in each sub-region by plotting their latitude-longitude distribution in four areas labeled "0" to "3". The labels "0", "1", "2" and "3" indicate, respectively, CR values with negligible total rotational energy, downward, LP and upward dominant GW energy flux. The relative coverage of each of them depends on the thresholds arbitrarily chosen to define the low-energy and linearly polarized GWs.

In the upper height interval, the total available GW energy per unit mass is, on average, five times larger than at lower levels. Also, both the total upward GW energy flux and the upward GW energy flux per unit area are weaker here than the respective downward magnitudes. This is contrary to what is observed in the lower height interval. The cumulative effect on C_R and E_T through the vertical wavenumber indicates upward and downward flows with significant deviations from linear polarization. These are observed east of the 75W meridian and in the

South Pacific. This is also observed in E_T. Regions with different degrees of polarization, where downward flows dominate, are systematically distributed in elongated bands. These are of different widths and have a predominantly NW-SE direction. These strips are also clear when labeled in four groups as described above.

The information to be extracted from the 3 coefficients, C_R, E_T and NC_R is in some sense, complementary. The features and conclusions drawn from each image shown in each one of the 6 attached videos are valid only for the corresponding harmonic and completely different from the remaining harmonics.

Finally, using the same IFS simulations, we analyze the phase difference between temperature and vertical wind. In doing so, we determine the vertical propagation direction of GWs in the lower height range based on the phase difference between the temperature and vertical wind disturbances. The relative increase of upward GWs with respect to downward GWs above and near the southern Andes and the Antarctic Peninsula, as well as their geographical distribution, is in agreement with our results in section 4.1.

A spectral rotary analysis from mesoscale numerical simulations exhibiting a four-dimensional context for the GWs is left for a future contribution. Recently, a study complementary to the one presented here and based on mesoscale simulations during flight 08 is provided by Alexander et al. (submitted). Version 4.2 of the ARW Weather Research and Forecasting (WRF) model is forced with initial and boundary conditions from the 0.25 x 0.25 degree ERA5 reanalyses provided hourly. Data are available at 137 levels from 1000 to 0.01 hPa. The solution has 150 vertical levels and the authors compare the model results with measurements obtained during SOUTHTRAC-GW. In particular, the possible coexistence and interaction of orographic and non-orographic gravity waves is evaluated.

Acknowledgments

AT, PA, RH, PL and TM were funded by grants ANPCYT PICT 2018-653 and PIP-CONICET20170100067

Open Research

References

Alexander, M. J. (1998). Interpretations of observed climatological patterns in stratospheric gavity wave variance, *J. Geophys. Res.*, 103, 8627–8640. https://doi.org/10.1029/97JD03325

Alexander, M. J., M. Geller, C. McLandress, S. Polavarapu, P. Preusse, Sassi, F., et al. (2010). Recent developments in gravity wave effects in climate models, and the global distribution of gravity wave momentum flux from observations and models, *Q. J. Roy. Meteorol. Soc.*, 136, 1103-1124, https://doi.org/10.1002/qj.637

Alexander, P., & de la Torre, A. (2010). A Method to Infer the Three Cartesian Wavelengths of a Mountain Wave from Three Soundings, *J. Appl. Meteor. Climatol.*, *49*, 2069–2074. https://doi.org/10.1175/2010JAMC2348.1

Alexander, P., de la Torre, A., Hierro, R., & Llamedo, P. (2015a). Assessment of precision in ionospheric electron density profiles retrieved by GPS radio occultations, *Adv. Space Res.*, http://dx.doi.org/10.1016/j.asr.2014.08.029, 54, 2249-258

Alexander, P., de la Torre, A., Schmidt, T., Llamedo, P., & Hierro, R. (2015b). Limb sounders tracking topographic gravity wave activity from the stratosphere to the ionosphere around midlatitude Andes, *J. Geophys. Res.*, 120. https://doi.org/10.1002/2015JA021409

Alexander, P., Schmidt T., & de la Torre, A. (2018). A method to determine gravity wave net momentum flux, propagation direction, and "real" wavelengths: A GPS radio occultations soundings case study. *Earth and Space Science*, *5*. https://doi.org/10.1002/2017EA000342

Alexander, P., et al. (2022). The coexistence of gravity waves from diverse sources during a SOUTHTRAC flight with optimal vertical propagation conditions. *J. Geophys. Res.*(to be submitted to this issue)

Bramberger, M., Dörnbrack A., Bossert K., Ehard B. , Fritts D.C., Kaifleret B., et al. (2017). Does strong tropospheric forcing cause large-amplitude mesospheric gravity waves? A DEEPWAVE case study. *J. Geophys. Res. Atmos.*, 122, 11 422–11 443. https://doi.org/10.1002/2017JD027371

779 Bramberger, M., Dörnbrack, A., Wilms, H., Ewald, F., & Sharman, R. (2020). Mountain-wave
780 turbulence encounter of the research aircraft HALO above Iceland. *J. Appl. Meteor.*
781 *Climatol.*,59, 567–588. https://doi.org/10.1175/JAMC-D-19-0079.1

782 Cadet, D., & Teitelbaum, H. (1979). Observational evidence of internal inertia-gravity waves in
783 the tropical stratosphere. *J. Atmos. Sci*., 36, 892-907

784 Cho, J.Y.N. (1995). Inertio-gravity wave parameter estimation from crossspectral analysis. *J*
785 *Geophys Res*, 100:18727–18737. https://doi.org/10.1029/95JD01752

786 Gill, A.E. (1982). Atmosphere and Ocean Dynamics, Academic Press, New York

787 Gubenko, V.N., Kirillovich1, I. A., & Andreev, V.E. (2020). Improvement of methods for
788 studying internal gravity waves in the Earth's atmosphere using radiosonde measurements, *J.*
789 *Phys.: Conf. Ser.* 1632 012007

790 Hertzog, A., Boccara, G., Vincent, R., Vial, F., & Cocquerez, P. (2008). Estimation of gravity
791 wave momentum flux and phase speeds from quasi-lagrangian stratospheric balloon Flights. Part
792 II: Results from the Vorcore Campaign in Antarctica, *J. Atmos. Sci.*, 65, 10, 3056-3070,
793 https://doi.org/10.1175/2008JAS2710.1

794 Hindley, N.P., Wright, C.J., Smith, N.D., & Mitchell, N.J. (2015). The southern stratospheric
795 gravity wave hotspot: individual waves and their momentum fluxes measured by COSMIC GPS-
796 RO, *Atmos. Chem. Phys.*, *15*, 7797–7818. https://doi.org/10.5194/acp-15-7797-2015

797 Hines, C.O. (1991). The saturation of gravity waves in the middle atmosphere. Part I: Critique of
798 linear instability theory, *J. Atmos. Sci.*, 48, 1348-1359

799 Hirota, I., & Niki, T. (1985). A Statistical Study of Inertia-Gravity Waves in the Middle
800 Atmosphere, *J. M. Soc. Jap*, 63, 6, 1055-1066

801 Hoffmann, L., Grimsdell, A. W., & Alexander, M. J. (2016). Stratospheric gravity waves at
802 Southern Hemisphere orographic hotspots: 2003 –2014 AIRS/Aqua observations, *Atmos. Chem.*
803 *Phys.*, *16*, 9381–9397. https://doi.org/10.5194/acp-16-9381-2016

804 Kaifler, N., Kaifler, B., Dörnbrack, A., Rapp, M., Hormaechea, J. L., & de la Torre, A. (2020).
805 Lidar observations of large-amplitude mountain waves in the stratosphere above Tierra del
806 Fuego, Argentina, *Sci. Rep.*, *10*, 14529. https://doi.org/10.1038/s41598-020-71443-7

807 Krisch, I., Preusse P., Ungermann, J., Dörnbrack, A., Eckermann, S.D., & Ern, M. (2017). First
808 tomographic observations of gravity waves by the infrared limb imager GLORIA. *Atmos. Chem.*
809 *Phys.*, **17**, 14 937–14 953. https://doi.org/10.5194/acp-17-14937-2017

810 Leaman, K. D., & Sanford, T. B. (1975). Vertical energy propagation of inertial waves: A vector
811 spectral analysis of velocity profiles, *l. Geophys.Res., 80,* 1975-1978.
812 https://doi.org/10.1029/JC080i015p01975

813 Lehmann, C. I., Kim, Y.H., Preusse, P., Chun, H.Y., Ern, M., & Kim, S.Y. (2012).
814 Consistency between Fourier transform and small-volume few-wave decomposition for spectral
815 and spatial variability of gravity waves above a typhoon. *Atmos. Meas. Tech.*, 5(7), 1637-1651.
816 https://doi.org/10.5194/amt-5-1637-2012

817 Llamedo, P., Salvador, J., de la Torre, A., Quiroga, J., Alexander, P., Hierro, R., et al. (2019). 11
818 years of Rayleigh lidar observations of gravity wave activity above the southern tip of South
819 America, *J. Geophys. Res. Atmos.*, *124,* 451–467. https://doi.org/10.1029/2018JD028673

820 Mishchenko, M. I. (2014). *Electromagnetic Scattering by Particles and Particle Groups: An*
821 *Introduction*, Cambridge University Press, Cambridge

822 Mooers, C. N. K. (1973). A technique for the cross spectrum analysis of pairs of complex-valued
823 time series, with emphasis on the properties of polarized components and rotational invariants,
824 *Deep Sea Reli., 20,* 1129-1141

825 Plougonven, R., & F. Zhang (2014). Internal gravity waves from atmospheric jets and fronts,
826 *Rev. Geophys.*, 52. https://doi.org/10.1002/2012RG000419

827 Polichtchouk, I., et al. (2021). Stratospheric Modelling and Assimilation, ECMWF Technical
828 Memorandum

Portele, T. C., Dörnbrack, A., Wagner, J. S., Gisinger, S., Ehard, B., Pautet, P.D., et al. (2018). Mountain-wave propagation under transient tropospheric forcing: A DEEPWAVE case study. *Mon. Wea. Rev.*, **146**, 1861–1888. https://doi. org/10.1175/MWR-D-17-0080.1

Rapp, M., Kaifler, B., Dörnbrack, A., Gisinger, S., Mixa, T., Reichert, R., et al. (2021). SOUTHTRAC-GW: An Airborne Field Campaign to Explore Gravity Wave Dynamics at the World's Strongest Hotspot. *Bull. Amer. Meteor.Soc., 102* (4), E871 - E893. https://doi. org/10.1175/BAMS-D-20-0034.1

Riese, M., Oelhaf, H., Preusse, P., Blank, J., Ern, M., Friedl-Vallon, F., et al. (2014). Gimballed Limb Observer for Radiance Imaging of the Atmosphere (GLORIA) scientific objectives. *Atmos. Meas. Tech.*, **7**, 1915–1928. https://doi.org/10.5194/amt-7-1915-2014

Skamarock, W., & J. B. Klemp (2008). A time-split nonhydrostatic atmospheric model for weather research and forecasting applications, *J. Comput. Phys.*, *227*, 3465–3485. https://doi. org/10.1016/j.jcp.2007.01.037

Smith, R. B., Nugent, A. D., Kruse, C. G., Fritts, D. C., Doyle, J. D., Eckermann, S. D., et al. (2016). Stratospheric Gravity Wave Fluxes and Scales during DEEPWAVE, Journal of the Atmospheric Sciences, 73(7), 2851-2869. https://doi.org/10.1175/JAS-D-15-0324.1

Vadas, S. L. (2013). Compressible *f*-plane solutions to body forces, heatings, and coolings, and application to the primary and secondary gravity waves generated by a deep convective plume, *J. Geophys. Res. Space Physics*, *118*, 2377–2397, doi:10.1002/jgra.50163

Vincent, R.A. (1984). Gravity-wave motions in the mesosphere, *J. Amos. Terr. Phys*., 46, 2, 119-128

Vincent, R.A., & Fritts, D.C. (1987). A Climatology of Gravity Wave Motions in the Mesopause Region at Adelaide, Australia, J. *Atmos. Sci.* https://doi.org/10.1175/15200469(1987)044<0748:ACOGWM>2.0.CO;2

Vincent, R. A., & Alexander, M. J. (2020). Balloon-borne observations of short vertical wavelength gravity waves and interaction with QBO winds. J. Geophys. Res.–Atmos., 125, e2020JD032779.https://doi.org/10.1029/2020JD032779

Wickert, J., Arras, C., Brack, A., Dick, G., Kepkar, A., Männel, B., et al. (2021). Ground and Space based GNSS for Space Weather Monitoring at GFZ: Overview and Recent Results - *Abstract Book, IAG* 2021

Wilms, H., Bramberger, M., & Dörnbrack, A. (2020). Observation and simulation of mountain wave turbulence above Iceland: Turbulence intensification due to wave interference. *Quart. J. Roy. Meteor. Soc.*, **146**, 3326–3346. https://doi.org/10.1002/qj.3848

Wu, D. L., Preusse, P., Eckermann, S.D., Jonathan, H. J., de la Torre, M.J., Coy, L., et al. (2006). Remote sounding of atmospheric gravity waves with satellite limb and nadir techniques, *Adv. Space Res.*, *37*, 22692277

Zhang, F., Wang, S., & Plougonven, R. (2004). Potential uncertainties in using the hodograph method to retrieve gravity wave characteristics from individual soundings, *Geophys. Res. Lett.*, 31 (L11110).https://doi.org/10.1029/2004GL019841